Multifunctional and Sensitivity Enhancement of Hybrid Acoustoplasmonic Sensors Fabricated on 36XY-LiTaO

by Teguh Firmansyah

Multifunctional and Sensitivity Enhancement of Hybrid Acoustoplasmonic Sensors Fabricated on 36XY-LiTaO$_3$ with Gold Nanoparticles for the Detection of Permittivity, Conductivity, and the Refractive Index

Teguh Firmansyah,* Gunawan Wibisono, Eko Tjipto Rahardjo, and Jun Kondoh*

Read Online

ACCESS | Metrics & More | Article Recommendations | Supporting Information

ABSTRACT: Integration of high-sensitivity sensors with multiple sensing performance for the environmental detection of permittivity (ε_r), conductivity (σ), and the refractive index (n) is required to support Societies 5.0. However, there are still many sensors with low sensitivity that stand alone. A shear horizontal surface acoustic wave (SH-SAW) sensor is usually used because of its high-sensitivity performance in detecting electrical properties. Moreover, localized surface plasmon resonance (LSPR) sensors show remarkable optical side capability. Here, we have successfully combined these advantages with an additional benefit of sensitivity enhancement. We propose a hybrid acoustoplasmonic sensor generated by integrating SH-SAW and LSPR devices to simultaneously detect ε_r, σ, and n. The SH-SAW sensor was fabricated on a 36XY-LiTaO$_3$ substrate using a developed interdigital transducer. Then, the LSPR sensor was implemented by the deposition of gold nanoparticles (AuNPs) on the propagation surfaces of the SH-SAW sensor. Fascinatingly, the AuNPs not only generate the LSPR effect but also enhance the SH-SAW sensor sensitivity. Comprehensive investigations were performed with atomic force microscopy imaging, CST software used for plasmonic E-field simulation, and hybrid sensing evaluation. Moreover, the SH-SAW sensitivity enhancement achieved using AuNPs was verified by frequency-domain and time-domain measurements. Thus, the SH-SAW sensor with AuNPs has a wide ε_r detection range (25−85), sensing capabilities for ultrasmall σ (0.0003−0.02504 S/m), and high sensitivity for n detection (45.5−201.9 nm/RIU). The cross-sectional effects were also evaluated. The effect of the LSPR device on the SH-SAW device was examined by turning the light OFF or ON (hereafter OFF/ON). The impact of the SH-SAW device on the LSPR device was investigated by turning the sine signal OFF/ON. We found that the SH-SAW sensor was not impacted by light. Interestingly, the presence of the SH-SAW sensor affects the positions of the AuNPs, which consistently generates a small blueshift in the LSPR effect. However, insignificant variation was noted in independent performances. In general, the SH-SAW sensor with AuNPs shows multifunctional independent characteristics and high-sensitivity performance, making it suitable for a chemical environment, with the possibility of integration with a wireless network.

KEYWORDS: *multifunctional sensor, SH-SAW, LSPR, permittivity sensor, conductivity sensor, refractive index sensor*

1. INTRODUCTION

In recent years, several studies have focused on designing multifunctional sensors for integrated and diverse applications[1−4] to support Societies 5.0. These multifunctional sensors have several advantages, such as low cost, low energy consumption, light weight, and containing massive information.[5,6] Several interesting materials and phenomena, such as ionic materials,[7,8] nanocarbon structures,[9] graphene oxide,[10−13] piezoelectric sensors based on zinc oxide materials,[14−17] film bulk acoustic wave resonators (FBARs),[18,19] quartz crystal microbalances (QCMs),[20,21] Rayleigh surface acoustic waves (R-SAWs),[22−26] and shear horizontal surface acoustic waves (SH-SAWs),[27−30] are
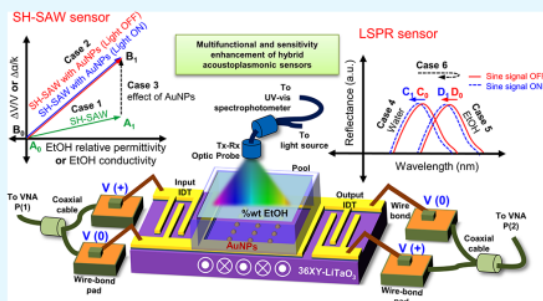
exploited to develop multifunctional sensors. In general, to produce multifunctional sensing performance, two or more devices should be combined. However, multifunctional sensing devices have several common problems, such as low sensitivity, slow response, weak electrocoupling, difficult fabrication
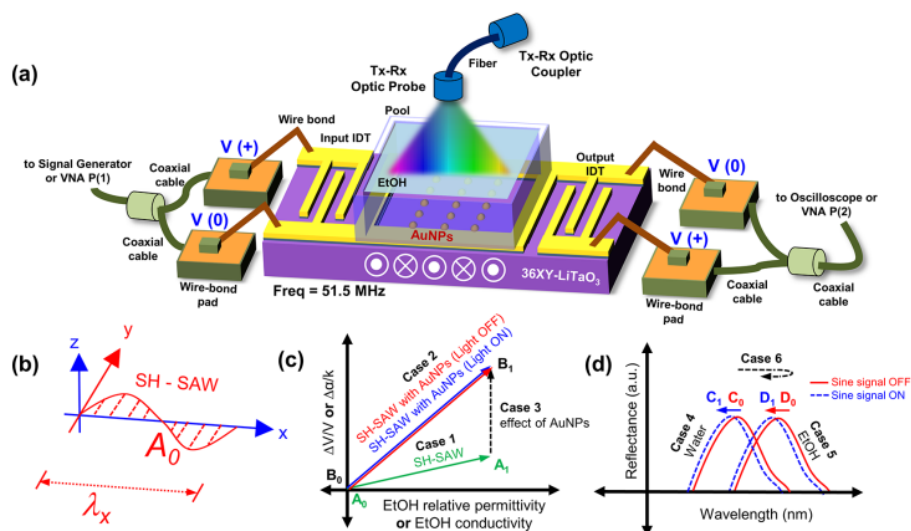
Figure 1. (a) Hybrid acoustoplasmonic multifunction sensor proposed by integrating an SH-SAW sensor with an LSPR device, (b) particle displacement of the SH-SAW device, (c) detailed case response of the acoustoelectric sensor investigation based on the SH-SAW evaluation, and (d) detailed case response of the plasmonic sensor investigation based on the LSPR evaluation.

processes, ease of breaking, unstable nanostructures in chemical environments, and immature technology.

To address these problems, a multifunctional sensor based on a piezoelectric substrate, such as FBAR, QCM, R-SAW, or SH-SAW, is usually utilized. Such a sensor has a large electromechanical coupling coefficient (K_s^2) and a high piezoelectric factor, leading to a large energy conversion coefficient from electrical to mechanical energies and vice versa.[31] In addition, it employs mature technology and fabrication techniques.[32,33] Pedro et al.[18] proposed a dual-mode thin-film FBAR with multiple longitudinals for temperature and mass loading sensing. This sensor was evaluated experimentally. Sternhagen et al.[19] proposed a combination of surface-skimming bulk-wave and SAW devices for integrated acoustic gas and temperature sensors. QCMs are another type of piezoelectric material sensor. Friedt et al.[21] proposed and combined a QCM sensor with a surface plasmon resonance (SPR) device for collagen/fibrinogen sensing. However, the SPR sensor has drawbacks, such as its need for a prism; therefore, the measured system is complex.

A multifunctional sensor based on the Rayleigh mode was proposed in refs.[22,26] A LiNbO$_3$ piezoelectric substrate is usually used to generate the Rayleigh mode, which is favorable for temperature sensors or gas applications. Renaudin et al.[24] proposed integrating an R-SAW device with a SPR sensor for microfluidic systems. R-SAW was utilized for active microfluidic mixing, and the SPR sensor was used for detection. The use of the R-SAW device accelerated the binding of the avidin-biotin assay. Moreover, R-SAW devices can be utilized for multifunctional sensors, such as pressure and temperature sensors[25] and physical quantity and temperature sensors.[26]

Other piezoelectric sensor devices of interest are SH-SAW sensors.[27–30] Their performance in liquid sensing applications is excellent. Furthermore, they have multifunctional capabilities for engine oil evaluation,[27] the detection of conductivity and pH in the liquid phase,[29] taste sensors,[34] permittivity sensors,[35] and monitoring the density and viscosity of liquids.[30] Okuda et

al.[28] proposed integrating an SH-SAW sensor on a LiTaO$_3$ substrate with a graphene field-effect transistor to create a graphene surface acoustic wave (GSAW) device. This hybrid GSAW sensor was successfully implemented and evaluated for simultaneous charge and mass detection. SH-SAW devices have several advantages, such as low power consumption, low cost, wireless control, and ability to operate in a liquid environment.[36] In brief, several interesting reports indicate that piezoelectric materials have significant potential to be combined with other devices to obtain multifunctional sensors.

As a novelty, we propose a hybrid acoustoplasmonic multifunctional sensor that integrates an SH-SAW device with a localized SPR (LSPR) device, as illustrated in Figure 1(a). In brief, the contributions of this study are as follows.

1. The proposed hybrid sensor device can simultaneously examine electrical and optical characteristics, such as relative permittivity (ε_r), conductivity (σ), and refractive index (n), with high sensitivity.
2. The SH-SAW sensor was fabricated on a 36XY-LiTaO$_3$ substrate using a developed interdigital transducer (IDT). Then, the LSPR sensor was developed by the deposition of gold nanoparticles (AuNPs) on the propagation surface of the SH-SAW device. The deposition of AuNPs on the propagation surface of the SH-SAW device not only generates the LSPR effect but also increases the SH-SAW sensor sensitivity. Next, we will refer to the hybrid device as the SH-SAW sensor with AuNPs.
3. The fundamental examination of the proposed SH-SAW sensor with AuNPs was performed by examining the performances of the two components, namely, the SH-SAW and LSPR devices. The performance of the SH-SAW sensor was evaluated based on the change in attenuation ($\Delta\alpha/k_0$) and change in velocity ($\Delta V/V$). This was followed by an examination of the performance of the LSPR sensor, in which the peak position (λ_p), wavelength shift ($\Delta\lambda$), and refractive index unit (RIU)

sensitivity were assessed. Ethanol (EtOH) (from 0 to 100% solutions with a step increase of 10%) was used as a liquid sample.

4. The deposition of AuNPs on the 36XY-LiTaO$_3$ substrate with annealing and quenching has dual beneficial functions. It not only generates the LSPR effect but also increases the sensitivity of the SH-SAW sensor.

5. Cross-sectional effects, such as LSPR to SH-SAWs and vice versa, were also evaluated. The effect of the LSPR device on the SH-SAW device was examined by turning the light source OFF/ON. In contrast, the effect of the SH-SAW device on the LSPR device was investigated by turning the sine signal from the signal generator OFF/ON. We found that the SH-SAW sensor was not impacted by light. Interestingly, the presence of the SH-SAW sensor led to the vibration of AuNPs, which consistently generated a small blueshift in the LSPR effect. However, an insignificant change was noted in the independent performances.

6. CST software was utilized to evaluate the E-field plasmonic distribution for a single AuNP and dimer AuNP on a 36XY-LiTaO$_3$ substrate in a liquid environment. Comprehensive experiments, such as atomic force microscopy (AFM), high-precision oscilloscope experiments, vector network analysis (VNA), and UV−vis spectrophotometry, were performed for surface imaging, time-domain evaluation, frequency-domain acoustoelectric sensing characterization, and plasmonic sensing investigation, respectively.

Finally, the proposed hybrid multifunctional sensor was successfully developed by integrating two mature technologies with several advantages, such as simultaneous detection with highly independent characteristics, good stability in a chemical environment, and a significant possibility of integration with a wireless network.

2. THEORY AND SIMULATION

The SH-SAW device based on the 36XY-LiTaO$_3$ substrate has a piezoelectric effect. The piezoelectric effect can convert an electric potential into mechanical stress and vice versa. An IDT structure should be used to excite the SH-SAW device. If an AC voltage is applied to the IDT, it produces an electric field. Thus, the electric field penetrates the 36XY-LiTaO$_3$ substrate and becomes stressed.

Figure 1(b) illustrates that the SH-SAW device demonstrates particle displacement in any direction. However, to analyze shear-horizontal waves, bulk waves are usually not considered because of high damping. Therefore, only the shear wave in the y-direction is examined. In brief, the particle displacement of the shear wave is described as follows:[36−38]

$$A(x, y, t) = A_0(y, t)e^{j\omega t - \gamma x} \tag{1}$$

where $A(x, y, t)$ is the particle displacement, A_0 the maximum amplitude of the particle displacement, ω is the angular frequency, and t is the time. The complex propagation coefficient wave γ is determined to be expressed as follows:[36−38]

$$\gamma = \alpha + jk_0 \tag{2}$$

where α is the attenuation and k_0 is the wavenumber. The wavenumber is calculated as follows:

$$k_0 = \frac{\omega}{V} \tag{3}$$

where V is the velocity of the SH-SAW sensor. The variations in wave propagation characteristics owing to different environments or additional loads, such as liquid samples at the propagation surface between input and output IDTs at a particular frequency, can be determined by the variations in the propagation coefficient.

$$\frac{\Delta\gamma}{k_0} = \frac{\Delta\alpha}{k_0} - j\frac{\Delta V}{V} \tag{4}$$

where $\Delta\gamma$ represents the change in the complex propagation coefficient. $\Delta V/V$ and $\Delta\alpha/k_0$ are impacted by changes in mass (m), viscoelastic constant (c), ε, σ, temperature (T), viscosity (η), density (ρ), and pressure (P). ΔV is determined as follows:[36−38]

$$\Delta V = \frac{\partial V}{\partial m}\Delta m + \frac{\partial V}{\partial c}\Delta c + \frac{\partial V}{\partial \varepsilon}\Delta\varepsilon + \frac{\partial V}{\partial \sigma}\Delta\sigma + \frac{\partial V}{\partial T}\Delta T$$
$$+ \frac{\partial V}{\partial \eta}\Delta\eta + \frac{\partial V}{\partial \rho}\Delta\rho + \frac{\partial V}{\partial P}\Delta P \tag{5}$$

Note that $\Delta\alpha$ is not a function of m. Therefore, $\Delta\alpha$ can be calculated as follows:[36−38]

$$\Delta\alpha = \frac{\partial \alpha}{\partial c}\Delta c + \frac{\partial \alpha}{\partial \varepsilon}\Delta\varepsilon + \frac{\partial \alpha}{\partial \sigma}\Delta\sigma + \frac{\partial \alpha}{\partial T}\Delta T + \frac{\partial \alpha}{\partial \eta}\Delta\eta$$
$$+ \frac{\partial \alpha}{\partial \rho}\Delta\rho + \frac{\partial \alpha}{\partial P}\Delta P \tag{6}$$

In our experiment, we used constant values of m, c, T, η, ρ, and P. A nonmetalized propagation surface loaded by a liquid sample was used so that $\Delta\varepsilon$ and $\Delta\sigma$ were not zero. Therefore, eqs 5 and 6 can be simplified as eqs 7 and 8, respectively:

$$\Delta V = \frac{\partial V}{\partial \varepsilon}\Delta\varepsilon + \frac{\partial V}{\partial \sigma}\Delta\sigma \tag{7}$$

$$\Delta\alpha = \frac{\partial \alpha}{\partial \varepsilon}\Delta\varepsilon + \frac{\partial \alpha}{\partial \sigma}\Delta\sigma \tag{8}$$

In brief, eqs 7 and 8 indicate that the values of $\Delta V/V$ and $\Delta\alpha/k_0$ are highly impacted by $\Delta\varepsilon$ and $\Delta\sigma$. Kondoh et al. successfully derived a detailed calculation of the $\Delta V/V$ and $\Delta\alpha/k_0$ an SH-SAW liquid sensor with electrical characteristics, such as relative permittivity and conductivity. The values of $\Delta V/V$ and $\Delta\alpha/k_0$ are calculated using eqs 9 and 10:[39,40]

$$\frac{\Delta V}{V} = -\frac{K_s^2}{2}\left[\frac{\left(\frac{\sigma'}{\omega}\right)^2 + \varepsilon_0(\varepsilon_r' - \varepsilon_r)(\varepsilon_r'\varepsilon_0 + \varepsilon_P^\tau)}{\left(\frac{\sigma'}{\omega}\right)^2 + (\varepsilon_r'\varepsilon_0 + \varepsilon_P^\tau)^2}\right] \tag{9}$$

$$\frac{\Delta\alpha}{k_0} = \frac{K_s^2}{2}\left[\frac{\left(\frac{\sigma'}{\omega}\right)(\varepsilon_r\varepsilon_0 + \varepsilon_P^\tau)}{\left(\frac{\sigma'}{\omega}\right)^2 + (\varepsilon_r'\varepsilon_0 + \varepsilon_P^\tau)^2}\right] \tag{10}$$

where σ' is the conductivity of the liquid sample, ε_0 is the vacuum permittivity, ε_r is the permittivity of the water or liquid reference, ε_r' is the permittivity of the sample liquid, ε_P^τ is the effective permittivity of the substrate used, and K_s^2 is the electromechanical coupling factor when a reference liquid is loaded on the surface. If ε_P^τ and ε_r are constant, we can see that the changes in $\Delta V/V$ and $\Delta\alpha/k_0$ are impacted only by the

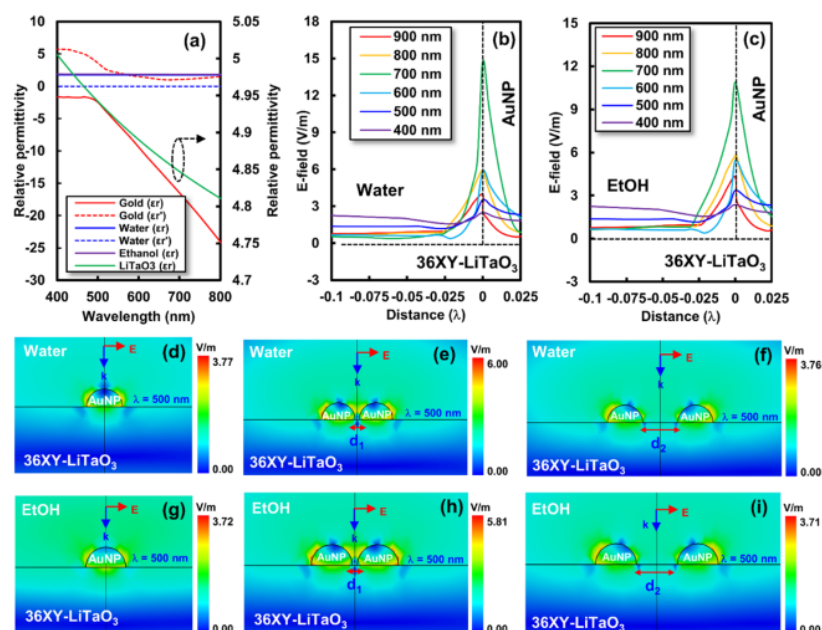**Figure 2.** (a) ε_r and $\varepsilon_{r'}$ from the CST simulation data; (b,c) simulation result of the E-field distribution at the AuNP on 36XY-LiTaO$_3$ for water and the 100 wt % EtOH medium, respectively; (d–f) 2D plasmonic E-field interaction among the 36XY-LiTaO$_3$ substrate, AuNP, and water medium at $\lambda = 500$ nm for a single AuNP, dimeric AuNPs with near (d_1) interdistances and dimeric AuNPs with far (d_2) interdistances, respectively; (g–i) 2D plasmonic E-field interaction among the 36XY-LiTaO$_3$ substrate, AuNP, and EtOH medium at $\lambda = 500$ nm for a single AuNP, dimeric AuNPs with d_1 interdistances, and dimeric AuNPs with d_2 interdistances, respectively.

values of σ', ε_r', and K_s^2. The values of σ' and ε_r' are dependent on the sample liquid. The value of K_s^2 is directly connected with the phase velocity of the SH-SAW, or it is inversely proportional to the time propagation (T_P) of the surface waves, as determined by eq 11:

$$K_s^2 \propto V \propto \frac{1}{T_P} \quad (11)$$

This means that even if ε_p^r, ε_r, σ', and ε_r' are constant, the final values of $\Delta V/V$ and $\Delta\alpha/k_0$ could be different because of the different K_s^2 values. K_s^2 is dependent on the surface propagation structure. The modified surface propagation structure can lead to higher/lower values of T_P, V, or K_s^2. In this study, the propagation structure was modified by the deposition of AuNPs in the middle of the propagation plane. This deposition leads to a lower value of T_P or higher values of V or K_s^2.

Details of the acoustoelectric sensor based on the SH-SAW device are presented in Figure 1(c). Case 1 (from A$_0$ to A$_1$) and case 2 (from B$_0$ to B$_1$) focused on the changes in the values of $\Delta V/V$ and $\Delta\alpha/k_0$ owing to the change in the liquid sample for the SH-SAW sensors without and with AuNPs, respectively. Moreover, case 3 (from A$_1$ to B$_1$) explained the change in the values of $\Delta V/V$ and $\Delta\alpha/k_0$ owing to the modification of the surface propagation structure. The effect of the light OFF/ON condition on the SH-SAW sensor with AuNPs was also investigated to observe the cross-sectional effect of the presence of light.

The LSPR effect was obtained if metal nanoparticles (MeNPs) such as gold, silver, and platinum nanoparticles

(AuNPs, AgNPs, and PtNPs) were deposited on a substrate such as glass or piezoelectric material and interacted with light. In this study, we generated LSPR by combining AuNPs, a 36XY-LiTaO$_3$ substrate, a water/EtOH liquid medium, and visible light ($r \ll \lambda$). The LSPR effect was analytically studied by Gustav Mie using Maxwell's equations.[41,42] He proposed several terms, such as scattering (σ_{sca}), extinction (σ_{ext}), and absorption (σ_{abs}) terms. The σ_{sca}, σ_{ext}, and σ_{abs} terms were determined as follows:[41,42]

$$\sigma_{sca} = \frac{32\pi^4\varepsilon_m^2 N_P^2}{\lambda^4}\frac{(\varepsilon_r - \varepsilon_m)^2 + (\varepsilon_{r'})^2}{(\varepsilon_r + 2\varepsilon_m)^2 + (\varepsilon_{r'})^2} \quad (12)$$

$$\sigma_{ext} = \frac{18\pi\varepsilon_m^{3/2}N_P}{\lambda}\frac{\varepsilon_{r'}(\lambda)}{[\varepsilon_{r'}(\lambda) + 2\varepsilon_m]^2 + \varepsilon_{r'}(\lambda)^2} \quad (13)$$

$$\sigma_{abs} = \sigma_{ext} - \sigma_{sca} \quad (14)$$

where ε_r and $\varepsilon_{r'}$ are the real and imaginary parts of the relative permittivity of the AuNPs, respectively. Therefore, N_P is the volume of the particle, and ε_m is the medium relative permittivity. Based on eqs 12–14, σ_{sca}, σ_{ext}, and σ_{abs} were highly dependent on ε_m, ε_r, $\varepsilon_{r'}$, and N_P. If ε_r, $\varepsilon_{r'}$, and N_P were constant, σ_{sca}, σ_{ext}, and σ_{abs} were determined by the value of ε_m for the medium. This characteristic was utilized for LSPR sensors, such as refractive index detectors.[43–46] Therefore, the changes in refractive index and its correlation with the changes in wavelength are expressed as follows:[47–49]

$$\Delta\lambda = S_r (n_m - n_r)[1 - e^{-2d_m/l_m}] \quad (15)$$

where $\Delta\lambda$ is the shift in wavelength, S_r is the sensitivity of the refractive index sensor, n_m is the refractive index of the

Table 1. Maximum E-Field Value and Skin Depth Position for Various Wavelengths and Surrounding Liquids

	AuNP and 36XY-LiTaO₃ substrate				
	water surrounding			EtOH surrounding	
wavelength (nm)	maximum E-Field (V/m)	$\delta_{36XY\text{-}LiTaO3 - Water}$ (λ)		maximum E-Field (V/m)	$\delta_{36XY\text{-}LiTaO3 - EtOH}$ (λ)
400	2.48	0.0092		2.36	0.0099
500	3.77	0.0046		3.72	0.0038
600	5.86	0.0021		5.42	0.0033
700	14.74	0.0017		10.88	0.0030
800	5.87	0.0060		5.77	0.0055
900	3.96	0.0075		4.30	0.0071

medium, n_r is the reference refractive index, d_m is the thickness of the dielectric medium, and l_m is the electromagnetic decay length characteristic of the sensor. For the bulk medium, S_r is usually simplified to eq 16:[47−49]

$$S_r = \frac{\Delta\lambda}{n_m - n_r} \tag{16}$$

Note that the presence of the SH-SAW device causes the AuNPs to move dynamically. This condition causes the interdistance of the AuNPs to fluctuate, leading to changes in the plasmonic E-field. The changes in the plasmonic E-field generate tunable LSPR.[50−54] In this study, we also investigated the tunable LSPR effect caused by the SH-SAW device on the performance of the LSPR sensor. The detailed scenario considered for the investigation of the performance of the LSPR sensor is described below.

As mentioned above, we developed an LSPR sensor through the deposition of AuNPs on an SH-SAW sensor with a 36XY-LiTaO₃ substrate and water/EtOH as a sample or liquid medium. Here, we used only the SH-SAW device with AuNPs because of the LSPR effect. In contrast, the SH-SAW sensor without AuNPs did not generate an LSPR response. The detailed case response of the SH-SAW device with AuNPs for LSPR sensor investigation is presented in Figure 1(d), that is, cases 4, 5, and 6. Cases 4 (from C_0 to C_1) and 5 (from D_0 to D_1) were evaluated for D_1 based on the impact of the OFF/ON sine signal on water and EtOH liquid samples, respectively. Case 6 (from C_0 to D_0 followed by D_1) focused on the change in the D_1 value owing to the change in the liquid sample consisting of mixtures with different concentrations of EtOH and water. Subsequently, the OFF/ON sine signal was also calculated for case 6, which was illustrated as the peak shifted from D_0 to D_1. Note that the OFF sine signal implies that SH-SAWs are not generated and vice versa.

CST software was used to evaluate the E-field plasmonic distribution at AuNPs on the 36XY-LiTaO₃ substrate with water/EtOH as a liquid medium. The software was developed based on a finite integration technique, that is, an algorithm based on a finite-difference time-domain (FDTD) function. It can be used for plasmonic calculation.[55,56] Before running the CST simulation, the ε_r and $\varepsilon_{r'}$ data of 36XY-LiTaO₃, water, EtOH, and AuNPs should be imported into the CST software database in the tabulated structure. The ε_r and $\varepsilon_{r'}$ data were acquired from ref.[57] and are represented graphically in Figure 2(a).

Figure 2(b,c) presents the simulation results of the E-field distributions at the AuNPs on 36XY-LiTaO₃ with the water or EtOH medium, respectively. The simulation was carried out from 400−900 nm as a function of the distance normalized by wavelength. The resonant behavior of AuNPs occurs at wavelengths of 500−600 nm. In this study, we can see that the maximum plasmonic E-field occurs at approximately 700 nm. This does not imply that the resonance of AuNPs shifted but implies that the maximum E-field at approximately 700 nm is an additional peak caused by 36XY-LiTaO₃ and AuNPs interacting with water or EtOH. The maximum plasmonic E-field at 700 nm is 14.74 V/m for the water medium and 10.88 V/m for the EtOH medium.

Different maximum plasmonic E-field values occur because of the different plasmonic characteristics of the liquid medium. Based on Figure 2(b,c), we can also determine the skin depth. Skin depth (δ) appears when the plasmonic E-field is equal to $1/e$ or 37% of the peak. The maximum plasmonic E-field value and the normalized skin depth position for different values of λ and different liquid media are summarized in Table 1. We can see that the maximum plasmonic E-field for the water medium was consistently higher than that for the EtOH medium for all wavelength values. A higher E-field value reduces the skin depth effect, which means that the E-field is focused on the surface area with a lower spread at depth. This condition occurs at the skin depth for 36XY-LiTaO₃−water ($\delta_{36XY\text{-}LiTaO3 - water}$) and 36XY-LiTaO₃ − EtOH ($\delta_{36XY\text{-}LiTaO3 - EtOH}$) for all wavelengths.

Figure 2(d−f) displays the 2D plasmonic E-field interactions among the 36XY-LiTaO₃ substrate, AuNPs, and water medium at λ = 500 nm for single AuNPs and dimer AuNPs with near (d_1) and far (d_2) interdistances, respectively. Figure 2(d) shows that the direct plasmonic E-field was produced at the single AuNP with a maximum plasmonic E-field of 3.77 V/m. When we added the second AuNP, generating the near-dimer AuNP structure depicted in Figure 2(e), the plasmonic E-field increased to 6.00 V/m. A larger plasmonic E-field value occurred because of the strong interaction between AuNPs, as illustrated by the orange color. However, if the interdistances among dimer AuNPs were increased, the plasmonic E-field returned to its initial value as a single AuNP structure, as displayed in Figure 2(f). It has a maximum plasmonic E-field of 3.76 V/m.

Figures 2(g−i) displays the 2D plasmonic E-field inter-actions among the 36XY-LiTaO₃ substrate, AuNP, and EtOH medium at λ = 500 nm for single AuNPs, dimer AuNPs with d_1 interdistances, and dimer AuNPs with d_2 interdistances, respectively. We can see that the plasmonic interaction in the EtOH medium has characteristics similar to those in the water medium. However, the value of the maximum plasmonic E-field obtained with the EtOH medium is lower than that obtained with the water medium: 3.72, 5.81, and 3.71 V/m for single AuNPs, dimeric AuNPs with d_1 interdistances, and dimeric AuNPs with d_2 interdistances, respectively. The difference in the maximum plasmonic E-field values occurred because of the different plasmonic characteristics of the liquid,
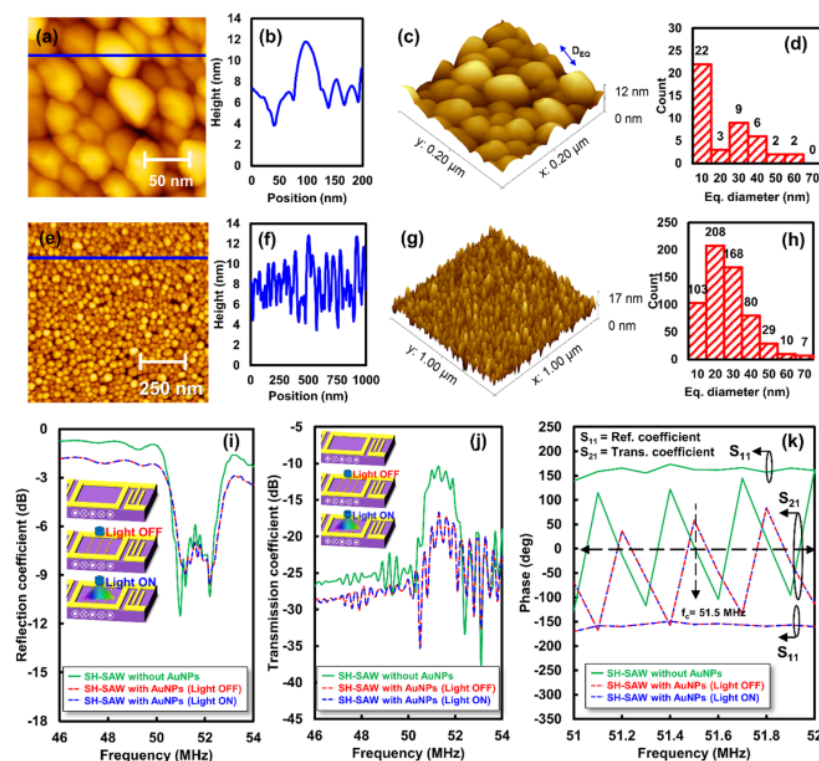
Figure 3. (a−d) Captured 2D AFM image with a size of 200 nm × 200 nm, the height of AuNPs at the line, the 3D surface of the AFM image, and the particle distribution, respectively. (e−h) Captured 2D AFM image with a size of 1000 nm × 1000 nm, the height of AuNPs at the line, the 3D surface of the AFM image, and the particle distribution, respectively. (i) Magnitude of S_{11}, (j) magnitude of S_{21}, and (k) comparison of the phase results of S_{11} and S_{21} for the SH-SAW sensor without AuNPs and SH-SAW sensor with AuNPs under light OFF/ON conditions.

such as the difference in the refractive index values. Several interesting things can be noted about this simulation result, such as the combination of AuNPs and the water/EtOH medium on the 36XY-LiTaO$_3$ piezoelectric substrate, generating a successful light-producing LSPR phenomenon. The different media produced different LSPR responses and could be used for various sensing devices. In addition, the plasmonic E-field value obtained for dimer AuNPs with longer distances was lower than that obtained for single AuNPs, which was caused by the long distance between AuNPs. Therefore, its dimer structure can be considered monomer AuNPs. Comparing the E-field values of the dimer (3.76 V/m) and monomer (3.77 V/m) shows that the values are equal, and there is not a significant differen. Moreover, if the AuNPs were dynamically moving owing to the presence of the SH-SAW device, the LSPR response would be slightly different. This characteristic will be explained in the section that describes the LSPR sensor evaluation.

3. RESULTS AND DISCUSSION

3.1. Morphological characterization. Figures 3(a−d) presents a captured 2D AFM image (of size 200 nm × 200 nm), the height of AuNPs at the line, the 3D surface of the AFM image, and the particle distribution, respectively.

In addition, the captured 2D AFM image of size 1000 nm × 1000 nm, height of AuNPs at the line, 3D surface of the AFM image, and particle distribution are presented in Figures 3(e−

h), respectively. Table 2 presents the AFM image surface analysis parameters of AuNPs on the 36XY-LiTaO$_3$ piezo-

Table 2. Surface Analysis Parameters of AuNPs, Such as the Amount of au Deposited, Annealing Conditions, Quenching Conditions, AFM Capture Size, Number of Particles (N), Maximum Height of the Surface (S_Z), Average Diameter Equivalent (D_{EQ}), and Interparticle Distance (ID) of AuNPs

AFM capture size (nm)	N	S_Z (nm)	D_{EQ} (nm)	ID (nm)
200 × 200	44	12	22.95	30.15
1000 × 1000	605	17	26.39	40.65

electric substrate, such as AFM capture size, number of particles (N), maximum height of surface (S_Z), average diameter equivalent (D_{EQ}), and interparticle distance (ID) of AuNPs. Based on the particle distribution chart, we can see that the IDs are approximately 30−40 nm, and they were calculated from center to center of the AuNPs. The diameters of the AuNPs (D_{EQ}) are from 10 to 70 nm. This size characteristic is significant because the LSPR effect will be generated if the particles are significantly smaller than the incident wavelength ($r << \lambda$).[41,42]

3.2. Scattering Parameters. Scattering parameters are generally used to describe the o of the scatter power.[58−61] The main parameters are the reflection coefficient (S_{11}) and transmission coefficient (S_{21}). S_{11} is the ratio between the
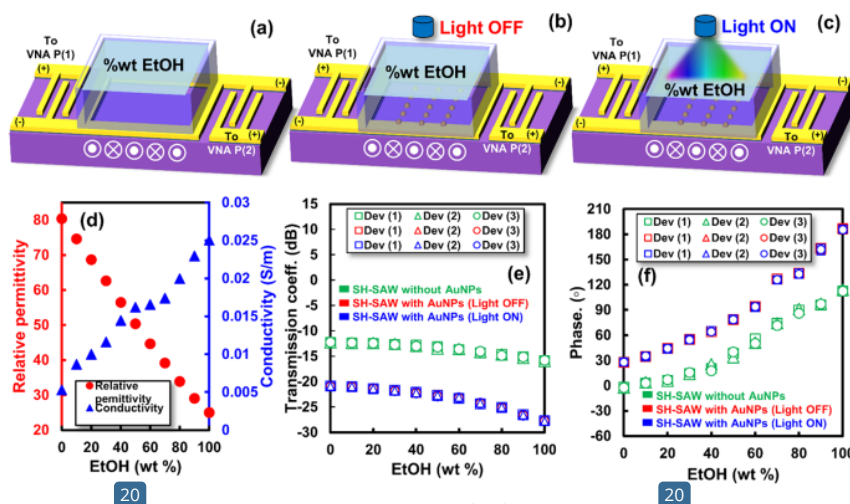
Figure 4. (a) Detailed position of the liquid sample for the SH-SAW sensor. (b, c) Detailed positions of the liquid sample for the SH-SAW device with AuNPs under light OFF and ON conditions, respectively. (d) σ and ε_r of EtOH at concentrations ranging from 0 to 100 wt %. (e, f) Magnitude and phase of the S_{21} of the SH-SAW sensor without AuNPs and SH-SAW sensor with AuNPs under light OFF/ON conditions after loading with the liquid sample, respectively.

reflected and input power, that is, $S_{11} = 10\log (P_{REF}/P_{IN})$, where P_{REF} is the reflected power and P_{IN} is the input power. S_{21} is the ratio between the output and input power, that is, $S_{21} = 10\log (P_{OUT}/P_{IN})$, where P_{OUT} is the output power. For the sensor evaluation, we should pay close attention to the frequency shift (Δf) of the highest value of the magnitude of S_{21} and the phase difference ($\Delta\theta$) of S_{21} at the same frequency or the center frequency. VNA is commonly used to measure the magnitude (dB) and phase ($^\circ$) of S_{11} and S_{21}.

Figure 3(i) displays the magnitude of S_{11} for the SH-SAW device without AuNPs and SH-SAW device with AuNPs under light OFF/ON conditions at frequencies of 46 and 54 MHz. We can see that the magnitudes of the S_{11} values are -7.32 and $-7.53/-7.52$ dB at a frequency of 51.5 MHz for the SH-SAW device without AuNPs and the SH-SAW device with AuNPs under light OFF/ON conditions, respectively. The result indicates that all magnitudes of S_{11} are small, which means that the electrical signal has successfully transferred from the signal generator to the device with low reflected power. Under the light OFF/ON condition, the result indicates that the S_{11} values are almost identical. Therefore, the OFF/ON light condition does not affect the S_{11} parameter of the SH-SAW device.

Figure 3(j) displays the magnitudes of S_{21} for the SH-SAW device without AuNPs and the SH-SAW device with AuNPs under light OFF/ON conditions between 46 and 54 MHz. The magnitude of S_{21} for the SH-SAW device without AuNPs at a frequency of 51.5 MHz is -11.91 dB. It has a larger S_{21} value than the SH-SAW device with AuNPs under light OFF/ON conditions, with values of -20.75 dB/-20.77 dB. We can see that the additional AuNPs on the surface of the SH-SAW device will change the transmission coefficient of the device. As mentioned above, for sensor evaluation, we should pay close attention to the frequency that generates the highest magnitude S_{21}. The highest magnitude S_{21} for the SH-SAW device without AuNPs was -11.02 dB at a frequency of 51.2 MHz, and the highest magnitude S_{21} for the SH-SAW device with AuNPs under the light OFF/ON condition was -16.66

dB/-16.67 dB at a frequency of 51.3 MHz. We can see that the frequency has shifted to a higher position. In Figure 3(k), the phase results of S_{11} and S_{21} are compared. The phase values at the central frequency of 51.5 MHz for the SH-SAW device without AuNPs and SH-SAW device with AuNPs under light OFF/ON conditions were 3.55° and $57.96^\circ/57.30^\circ$, respectively. The SH-SAW device with AuNPs produced a larger phase value.

In summary, from Figures 3(i–k), we can explain the S-parameter in terms of two main comparisons: the comparison of the SH-SAW device without AuNPs and the SH-SAW device with AuNPs and the comparison of the SH-SAW device with AuNPs only under light OFF and light ON conditions. In the initial comparison, there were insignificant changes in the magnitude of S_{11}. The results indicated that P_{REF} was low for both devices. Even though S_{11} was not the main parameter for the sensor examination, it was essential to ensure that the electric signal was successfully transmitted to the device with minimal reflection.

The main part of the sensor characteristics was evaluated by examining the variations in the magnitude and phase of S_{21}. We can see the different magnitudes and phases of the S_{21} results for the SH-SAW device without AuNPs and the SH-SAW device with AuNPs. The SH-SAW device without AuNPs produced a higher S_{21} magnitude than the SH-SAW device with AuNPs and also had a different S_{21} phase value. In particular, the SH-SAW device with AuNPs under light OFF/ON conditions has a higher frequency and larger phase value than the SH-SAW device without AuNPs. On the other hand, the SH-SAW device with AuNPs under light OFF/ON conditions had a higher velocity. From this preliminary result, we can safely say that the sensor devices have different characteristic sensing performances owing to their different initial results. A detailed evaluation of the sensing performance and its characteristics for different loaded liquid samples will be described in the following section.

For the second comparison, we can see similar results for the magnitude and phase of S_{11} and S_{21} under the light OFF/ON
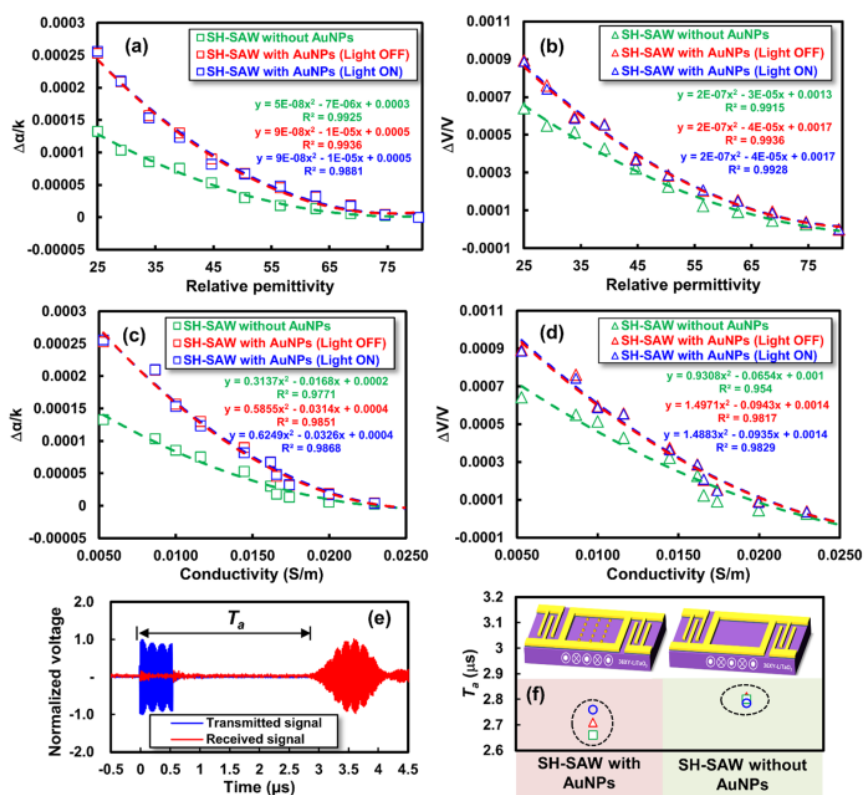
Figure 5. (a, b) Details of $\Delta\alpha/k_0$ and $\Delta V/V$ for different εr values; (c, d) details of $\Delta\alpha/k_0$ and $\Delta V/V$ for different σ value, respectively; (e) proposed time-domain measurement; and (f) comparison of the T_a values of the SH-SAW sensor without AuNPs and SH-SAW sensor with AuNPs.

condition. The results indicate that light was not impacted by the electrical result of the SH-SAW device. This occurred because neither the 36XY-LiTaO$_3$ substrate nor AuNPs were photoresistive or photoelectric materials. The separated and uncorrelated condition is an advantage in producing an independent multifunctional sensor.

3.3. SH-SAW Sensors without and with AuNPs. The performance of the SH-SAW sensor was evaluated based on the changes in $\Delta\alpha/k_0$ and $\Delta V/V$. The $\Delta\alpha/k_0$ and $\Delta V/V$ data were calculated from the VNA system that was connected to the SH-SAW sensor without AuNPs and the SH-SAW sensor with AuNPs. Commonly, the VNA system has an input power of 0 dBm or 1 mW, and SH-SAWs are generated. In this study, ethanol (EtOH) (from 0−100 wt % with a step increase of 10 wt %) was used as a liquid sample. Distilled water was used to dilute EtOH from higher to lower concentrations. Note that 0 wt % EtOH means distilled water and 100 wt % EtOH means pure EtOH without additional water. The liquid sample was placed in a silicon pool that was constructed at the center of the device. Figure 4(a−c) depicts the detailed positions of the liquid samples for the SH-SAW device without AuNPs and the SH-SAW device with AuNPs under light OFF and light ON conditions, respectively. The effects of the light OFF and light ON conditions were also examined to determine the impact of the presence of light on the acoustoelectric sensor, as depicted in Figure 4(b,c), respectively.

Before the performances of the SH-SAW sensor without AuNPs and the SH-SAW sensor with AuNPs were investigated, the electrical characteristics of the liquid sample were measured. Figure 4(d) displays the σ and ε_r of EtOH from 0−100 wt %. The σ of EtOH was measured using a CM-40 S conductive system (Toa, Japan), and ε_r was obtained from ref.[62] The values of ε_r were 80.73 and 25.00 for 0 and 100 wt % EtOH, respectively. The σ values were 0.00528 and 0.02504 S/m for 0 and 100 wt % EtOH, respectively.

Figure 4(e) depicts the magnitude of S_{21} for the SH-SAW sensors without and with AuNPs under light OFF/ON conditions after loading with the liquid sample. To obtain robust data, we used three devices: Dev (1), Dev (2), and Dev (3). In particular, the magnitudes of S_{21} for the SH-SAW sensor without AuNPs and SH-SAW sensor with AuNPs under the light OFF/ON condition were −12.25 dB and −20.88 dB/−20.85 dB for 0 wt % EtOH and −15.78 dB and −27.68 dB/−27.67 dB for 100 wt % EtOH, respectively. A comparison of the magnitudes of S_{21} for different EtOH concentrations and devices is plotted in Figure 4(e). Several interesting things can be noted about this result. First, compared to the SH-SAW device, the SH-SAW sensor with AuNPs under light OFF/ON conditions has a smaller S_{21} value at 0 wt % EtOH or the starting value. However, the difference in magnitude (ΔS_{21}) for the SH-SAW device without AuNPs is lower than that for SH-SAW sensor with AuNPs under light OFF/ON conditions

from 0 wt % EtOH to 100 wt % EtOH, with values of −3.35 dB and −6.80 dB/−6.82 dB, respectively. The results indicate that the deposition of AuNPs on 36XY-LiTaO$_3$ makes the sensor more responsive to changes in the liquid sample. Moreover, we can also see that the presence of light does not impact the performance of the acoustoelectric sensor.

As mentioned above, in addition to the magnitude of S_{21}, the S_{21} phase is also significant for sensing characterization. Figure 4(f) depicts the phases of the SH-SAW sensor without AuNPs and SH-SAW sensor with AuNPs under light OFF/ON conditions after loading with the liquid sample. The phases of the S_{21} values for the SH-SAW sensor without AuNPs and the SH-SAW sensor with AuNPs under light OFF/ON conditions are −2.39° and 27.85°/27.87° for 0 wt % EtOH, respectively. Meanwhile, the phases of the S_{21} values for the SH-SAW sensor without AuNPs and SH-SAW sensor with AuNPs under light OFF/ON conditions were 112.40° and 185.32°/185.31° for 100 wt % EtOH, respectively. The phase of the S_{21} values corresponds to the SH-SAW sensor without AuNPs and SH-SAW sensor with AuNPs under light OFF/ON conditions. The other phase results for the different liquid concentrations are presented in Figure 4(f).

In accordance with the S_{21} magnitude changes, the phase changes of S_{21} also have similar results. The SH-SAW sensor with AuNPs under light OFF/ON conditions had a $\Delta\theta$ value of 157.47°/157.46°, which is larger than the $\Delta\theta$ value for SH-SAW of 144.79°. In short, the additional AuNPs on the SH-SAW sensor produce larger ΔS_{21} and $\Delta\theta$ values than the SH-SAW sensor without AuNPs. This result is favorable because the proposed sensor or SH-SAW sensor with AuNPs is more reactive to the different characteristics of the liquid samples. Moreover, the OFF/ON light condition is not affected by the response of the SH-SAW sensor with AuNPs, which indicates the great independence of the acoustoelectric sensor.

Figure 5(a,b) presents $\Delta\alpha/k_0$ and $\Delta V/V$ for the relative permittivity of EtOH, respectively. For 0 wt % EtOH, $\varepsilon_r = 80$, which is equal to that of water, and for 100 wt % EtOH, $\varepsilon_r = 25$. In this study, we used water as the reference liquid. Therefore, the initial value or starting point of $\Delta\alpha/k_0$ and $\Delta V/V$ will be the same at a high ε_r value or for the liquid water reference.

In particular, Figure 5(a) illustrates the changes in the $\Delta\alpha/k_0$ value by varying ε_r from 25 to 80. We can see that at $\varepsilon_r = 80$, the value of $\Delta\alpha/k_0$ for the SH-SAW sensor with AuNPs under the light OFF/ON condition is zero because we use this point as the reference position. After we gradually decreased ε_r to 25 with an increase in EtOH concentration, we could see that the final $\Delta\alpha/k_0$ values were 0.00013 and 0.00025/0.00025 for the SH-SAW sensor without AuNPs and SH-SAW sensor with AuNPs under light OFF/ON conditions, respectively. Figure 5(a) presents further details of the $\Delta\alpha/k_0$ value for different values of ε_r. We can also see the trend line equation and value of R^2 that fit the data points. The R^2 values are 0.9925 and 0.9936/0.9881 for the SH-SAW sensor without AuNPs and SH-SAW sensor with AuNPs under light OFF/ON conditions, respectively. Figure 5(b) presents $\Delta V/V$ curves for different values of ε_r. We can see that at the highest concentrations of EtOH, $\varepsilon_r = 25$ and $\Delta V/V = 0.00064$ and 0.00088/0.00088, with R^2 values of 0.9915 and 0.9936/0.9828, respectively, corresponding to the SH-SAW sensor without AuNPs and SH-SAW sensor with AuNPs under light OFF/ON conditions, respectively.

Figures 5(c,d) depicts $\Delta\alpha/k_0$ and $\Delta V/V$ for σ EtOH, respectively. The conductivity of 0 wt % EtOH was 0.0250 S/m or equal to that of water and that of 100 wt % EtOH was 0.0050 S/m. The zero points of $\Delta\alpha/k_0$ and $\Delta V/V$ occur in water. In detail, Figure 5(c) depicts $\Delta\alpha/k_0$ for different values of σ. At the lowest value of σ, $\Delta\alpha/k_0 = 0.00017$ and 0.00025/0.00025 and $R^2 = 0.9771$ and 0.9851/0.9868 for the SH-SAW sensor without AuNPs and SH-SAW sensor with AuNPs under light OFF/ON conditions, respectively. Figure 5(d) displays $\Delta V/V$ for different values of σ. $\Delta V/V = 0.00024$ and 0.00088/0.00088 and $R^2 = 0.9540$ and 0.9817/0.9829 for the SH-SAW sensor and SH-SAW sensor with AuNPs under light OFF/ON conditions, respectively.

Several interesting points can be noted from Figure 5(a−d). The starting points or zero points of $\Delta\alpha/k_0$ and $\Delta V/V$ are the highest values of ε_r and σ, 80 and 0.0250 S/m, respectively. After deriving the trend line equation, we found that all the R^2 values were higher than 0.90, indicating that the trend line has a very good fit to the data point. The OFF/ON light condition did not change the $\Delta\alpha/k_0$ and $\Delta V/V$ values. These data are significant, as they indicate the independence of the acoustoelectric SH-SAW sensor with the AuNPs in the presence of light.

In Figure 5(a−d), all the green lines represent case 1 or the SH-SAW devices. The red and blue lines represent case 2 or the SH-SAW sensor under the light OFF/ON condition. We can see that the values of $\Delta\alpha/k_0$ and $\Delta V/V$ for case 1 are always consistently lower than $\Delta\alpha/k_0$ and $\Delta V/V$ for case 2. Finally, the difference values of $\Delta\alpha/k_0$ and $\Delta V/V$ for the SH-SAW sensor without AuNPs and SH-SAW sensor with AuNPs under the light OFF/ON condition for the lowest values of ε_r and σ, 25 and 0.0050 S/m, respectively, are represented by case 3. Figure 1(b) depicts the three cases.

Case 3 was unique, even when the liquid sample had the same concentration. The final values of $\Delta\alpha/k_0$ and $\Delta V/V$ were different. Based on the model proposed in eq 11, derived from eqs 9 and 10, even the liquid sample was constant. The final values of $\Delta\alpha/k_0$ and $\Delta V/V$ can be different owing to the different characteristics of the device, such as K_s^2. We found that the deposition of AuNPs at the propagation surface increased K_s^2. To prove this parameter, we proposed a time-domain measurement, as depicted in Figure 5(e).

The time-domain measurement was prepared by a sinusoidal signal with a frequency of 51.5 MHz and modulated with a single pulse signal. The signal is usually termed the amplitude shift keying (ASK) signal. We used the ASK signal as an input signal, and it was divided into two equal parts using a power divider. The first signal was directly connected to an oscilloscope and is known as a transmitted signal. The second signal was connected to the input IDT of the device, and then, the output IDT was connected to the oscilloscope and used as the received signal. The time-domain measurement data can be made robust in several ways. The power divider should have a low reflected signal intensity to avoid undesired mixed signals, the cable and connector should have constant parameters for repeatable measurements, and the oscilloscope should have good sensitivity. The time-domain signal result is presented in Figure 5(f). In brief, the time of arrival (T_a) is the difference in time between signal transmission and signal receipt. We now compare the T_a values of the SH-SAW sensor without AuNPs and SH-SAW sensor with AuNPs. The average T_a for the SH-SAW sensor without AuNPs is 2.798 μs, and the average T_a for
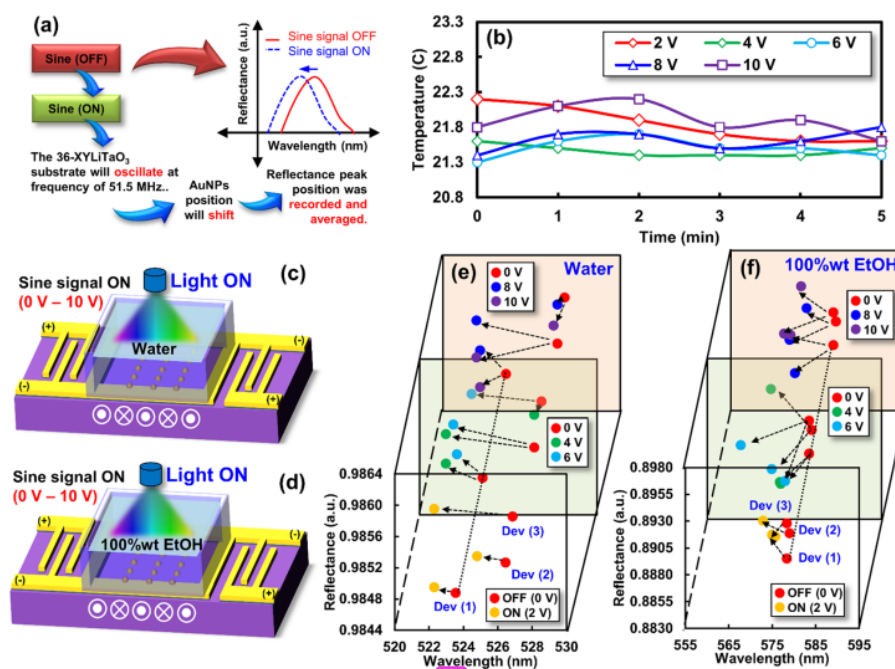
Figure 6. (a) Procedure used to examine the tunable LSPR effect. (b) Temperature of the SH-SAW sensor with AuNPs during the experiment; (c, d) Proposed LSPR measurement strategy for water and EtOH samples, respectively; and (e, f) reflectance value and wavelength shift with different sine signal voltages from 0 to 10 V for water and 100 wt % EtOH, respectively.

the SH-SAW sensor with AuNPs is 2.710 μs. Using an identical supporting measurement system, a lower value of T_a implies a higher value of V or K_s^2. In brief, we can say that the deposition of AuNPs on the surface with annealing and quenching will increase K_s^2. The increase in K_s^2 was proven in several ways, such as the frequency-domain measurement and time-domain measurement of the T_a value. Moreover, for more general results, optimization to increase the velocity is needed. This could be achieved by varying the annealing temperature, quenching method, and size or structure of AuNPs. Then, its effect could be investigated by simulation or time-domain and frequency-domain measurements.

3.4. Tunable LSPR Using the SH-SAW Sensor with AuNPs on a Liquid. As mentioned above, the SH-SAW sensor produces a dynamic LSPR effect owing to the acoustic movement of AuNPs. Therefore, an investigation of the tunable LSPR effect should be conducted, and the complete procedure is shown in Figure 6(a). The experiment was carried out at the room temperature of 23.5 C and humidity of 48%. Moreover, the temperature of the SH-SAW sensor with AuNPs was also investigated, as shown in Figure 6(b). We can see that the temperature during the experiment was stable at approximately 21.3 and 22.3 C. Therefore, we can conclude that the effect of temperature on the SH-SAW sensor with AuNPs is small. Figure 6c,d depicts the proposed LSPR measurement strategy. Water was used as a sample for the SH-SAW sensor with AuNPs. It was located at the sensing area or center of the propagation surface, on which the AuNPs were deposited. A silicon pool was used to hold a liquid sample, as depicted in Figure 6c,d for the water and 100 wt % EtOH samples, respectively. For this measurement, we used two variables, namely, the liquid sample concentration and input

voltage. In brief, an EtOH sample with concentrations increasing from 0 to 100 wt % with a step of 10 wt % was utilized as the liquid sample. In addition, the amplitude of the input sine signal was varied from 0 to 10 V with a step size of 1 V.

Figure 6(e,f) depicts the reflectance value and wavelength shift for different amplitudes from 0 to 10 V for water and 100 wt % EtOH, respectively. Figure 6(e) shows that the peak position for water is approximately 524−527 nm at 0 V. The zero voltage indicates that the SH-SAW does not appear. However, after we turn on the signal generator, we can see the peak position shifting. This condition was obtained because of the presence of the SH-SAW device. The SH-SAW device synchronously stimulates the dynamic movement of AuNPs. Therefore, the dynamically moving AuNPs produced a tunable LSPR effect.

The amplitude and frequency of the SH-SAW vibration are proportional to the sine signal's input voltage and frequency. The investigation of dynamic LSPR required a highly synchronous time between light capture and the frequency of SH-SAWs to consider light reflection with high precision. However, our laboratory does not yet have the tools to retrieve these data. We proposed another robust investigation method, such as comparing to 0 V, to examine the dynamic tunability of LSPR. Using this method, we successfully obtained robust and stable data regarding the dynamic tunability of LSPR. We can see that the peak position of the reflection has a consistent blueshift. Figure 6(e,f) depicts the details of the peak reflection shift with different voltages compared to those at 0 V in water and 100 wt % EtOH liquid, respectively. Figures S1(a−c), S2(a−c), and S3(a−c) depict the peak reflection shifts at various voltages for various concentrations of EtOH. In brief,
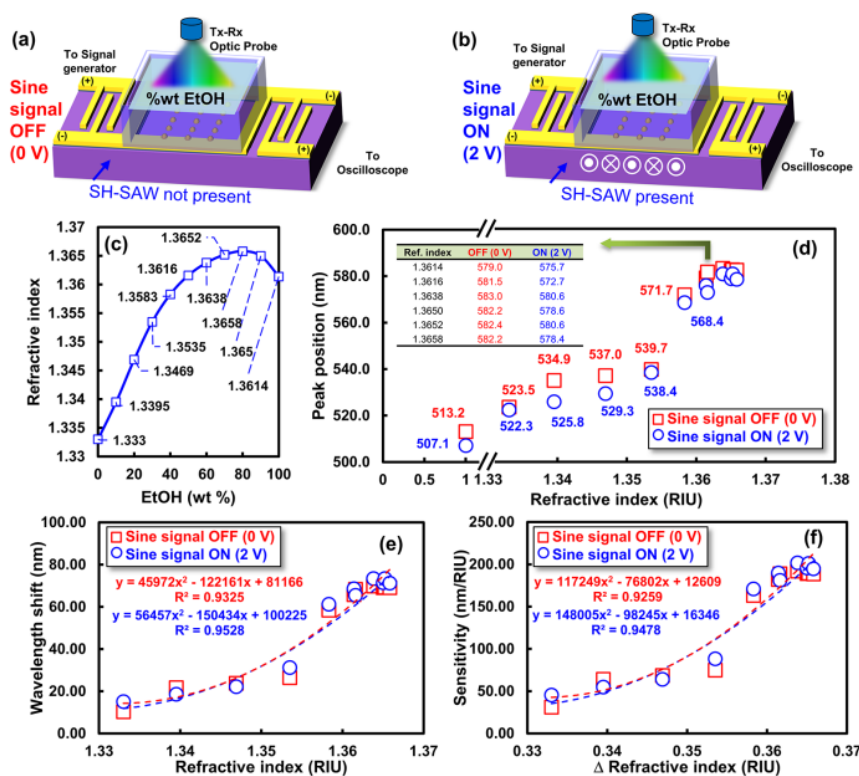
Figure 7. (a, b) LSPR sensor evaluation with different EtOH concentrations under sine signal OFF (0 V) and ON (2 V) conditions, respectively. (c) Correlation between the EtOH concentration and refractive index (n) value. (d) n value and its peak position under OFF (0 V) and ON (2 V) conditions. (e) Correlation between the n value and $\Delta\lambda$. (f) S_r of the LSPR sensor for the OFF and ON sine signals.

we found several interesting results. First, the SH-SAW stimulates the dynamic movement of AuNPs, and the motion of the AuNPs generates dynamic plasmonic E-field values. Therefore, the difference in the plasmonic E-field values produces tunable LSPR. Using the OFF/ON sine signal comparison strategy, we can see from the robust tunable LSPR data that the peak position has a consistent blueshift. After we increased the EtOH concentration of the liquid sample, a redshift in LSPR occurred. Thus, turning on the voltage source will produce a blueshift. Therefore, there are two simultaneous shifts, a redshift and a blueshift, because of the higher EtOH concentrations and the presence of the SH-SAW device. The effect of the simultaneous shifts on the LSPR sensor characteristics was investigated as follows.

3.5. LSPR Sensor Using the SH-SAW Sensor with AuNPs. As mentioned above, the LSPR effect is generated only by the SH-SAW device with AuNPs. Therefore, the investigation of LSPR sensor performance for refractive index detection was carried out only on the SH-SAW device with AuNPs. However, we should pay attention to the existence of the SH-SAW sensor and its effect on the LSPR sensor. Figure 7(a,b) depicts the LSPR sensor evaluation considering the difference in EtOH concentrations under the sine signal OFF (0 V) and ON (2 V) conditions, respectively. The OFF condition of the sine signal indicates that the SH-SAW sensor does not exist and vice versa. The LSPR sensor functions as a refractive index detector. Figure 7(c) depicts the correlation

between the EtOH concentration and the refractive index n. The n data were acquired from ref.[62] The n values of air, water, and 100 wt % EtOH were 1.000, 1.333, and 1.3614, respectively. The maximum n value of 1.3658 occurs at 80 wt % EtOH. Figure 7(d) depicts the n value and its peak position under OFF (0 V) and ON (2 V) conditions. We can see that a higher n value will increase the position of λ. It would be interesting to extend the discussion by comparing Figure 1(d) and Figure 7(d). Case 4 occurred for the water response under OFF (0 V) and ON (2 V) conditions, representing positions C_0 (523.5 nm) and C_1 (522.3 nm), respectively. Case 5 was applied for the EtOH result response, with characteristics similar to those of case 4. Finally, case 6 has a unique characteristic, in which the shift from C_0 (water, OFF, 523.5 nm) to D_0 (80 wt % EtOH, OFF, 582.2 nm) is caused by an increase in n, followed by the shift from D_0 (80 wt % EtOH, OFF, 582.2 nm) to D_1 (80 wt % EtOH, ON, 578.4 nm) caused by the SH-SAW sensor.

Figure 7(e) presents the correlation between n and $\Delta\lambda$. The value of $\Delta\lambda$ was obtained by comparing the peak position of the sample with that of air ($n = 1.000$). $\Delta\lambda$ was plotted under the OFF sine and ON sine signal conditions. It is essential to see the effect of the SH-SAW on $\Delta\lambda$. The trend lines of the $\Delta\lambda$ values on the OFF and ON sine signals were plotted simultaneously. We can see that the trend lines have similar curves and almost fit each other. The R^2 values obtained for the OFF and ON sine signal conditions were 0.93 and 0.95,

Table 3. Comparison of the Sensitivity of the Standalone and Multifunctional Sensors[a]

ref	device	method	electric signal ON	light ON	conductivity sensor sensitivity (× 10³) (1/(S/m)) $\left\|\dfrac{\Delta\alpha/k}{\Delta\sigma}\right\|$	$\left\|\dfrac{\Delta V/V}{\Delta\sigma}\right\|$	permittivity sensor sensitivity (× 10⁶) dimensionless $\left\|\dfrac{\Delta\alpha/k}{\Delta\varepsilon_r}\right\|$	$\left\|\dfrac{\Delta V/V}{\Delta\varepsilon_r}\right\|$	refractive index sensor sensitivity (nm/RIU) $\|S_r\|$
29	SH-SAW (51 MHz)	acoustic	yes	NA	1.71	1.36			
34	SH-SAW (50 MHz)	acoustic	yes	NA	2.50	12.0			
33	SH-SAW (30 MHz)	acoustic	yes	NA	5.00	30.0			
32	SH-SAW (100 MHz)	acoustic	yes	NA			2.55	10.6	
35	SH-SAW ($\sigma'/f = 1$)	acoustic	yes	NA			5.00	13.0	
43	Si/Quartz with AuNPs	plasmonic	NA	yes					87.8
	Si/Quartz with AuNPs annealing	plasmonic	NA	yes					116.8
44	glass with AuNPs	plasmonic	NA	yes					21.1−81.2
45	glass with AuNPs	plasmonic	NA	yes					34−48
	glass with AuNPs and immobilized	plasmonic	NA	yes					68
46	glass with AuNPs	plasmonic	NA	yes					70−100
75	glass AuNPs	plasmonic	NA	yes					40−90.8
	glass AuNPs with annealing quenching	plasmonic	NA	yes					103.6−240.4
76	glass Au Nanoisland	plasmonic	NA	yes					93
	glass Au Nanoisland annealing	plasmonic	NA	yes					114
This work	SH-SAW	acoustic	yes	NA	6.50	32.0	2.36	11.6	
	SH-SAW with AuNPs	acoustic	yes	OFF	12.5	44.0	4.55	16.0	
		plasmonic	OFF	yes					31.1−192.0
		hybrid acoustic-plasmonic	yes	yes	12.5	44.0	4.55	16.0	45.5−201.9

[a]NA = not applicable

respectively. R^2 indicates that the trend line has a good fit to the data point. Figure 7(f) depicts the S_r of the LSPR sensor for the OFF and ON sine signals. We can see that both curves have the same route. The presence of the SH-SAW sensor did not significantly impact the performance of the LSPR sensor.

Finally, Table 3 compares the sensitivity of the standalone or multifunctional sensor. We can see that the hybrid sensor has good sensitivity performance and multifunctional capability. Moreover, compared to the SH-SAW sensor without AuNPs, the SH-SAW sensor with AuNPs has better sensitivity characteristics.

Note that the SH-SAW sensor sensitivity is affected not only by AuNPs but also by the annealing temperature,[63−67] quenching, and the propagation structure of the SH-SAW sensor.[68−71] Similar to the SH-SAW sensor sensitivity, the LSPR sensor sensitivity is also affected by the size, distance, and structure of the nanoparticle and its interaction with the medium.[72−74] In addition, the simulation of AuNPs with different radii is shown in Figure S4(a) for the air medium and Figure S4(b) for the EtOH liquid, Figure S4(c) shows the σ_{abs} values, and Figure S4(d) shows the sensitivity effect. Simulation of the dimer AuNPs with different distances is shown in Figure S4(e) for air and Figure S4(f) for the EtOH liquid, Figure S4(g) shows the σ_{abs} values, and Figure S4(h) shows the sensitivity effect. Simulation of the AuNPs with a trimer structure is shown in Figure S4(i) for air and Figure S4(j) for the EtOH liquid, Figure S4(k) shows the σ_{abs} value, and Figure S4(l) shows the sensitivity effect. Overall, on the basis of this interesting finding, we successfully developed and investigated a hybrid acoustoplasmonic sensor with multifunc-tional, simultaneous, high-sensitivity, and independent performance.

4. CONCLUSIONS

In conclusion, a hybrid acoustoplasmonic multifunctional sensor with high sensitivity was successfully implemented. The sensor can simultaneously detect ε_r, σ, and n. The SH-SAW sensor was fabricated on a 36XY-LiTaO₃ substrate by developing IDTs. The LSPR sensor was implemented by the deposition of AuNPs in the middle of the surface propagation plane the SH-SAW sensor. The deposition of AuNPs on the propagation surface of the SH-SAW sensor with annealing and quenching not only generates the LSPR effect but also increases the SH-SAW sensor sensitivity. The increase in SH-SAW sensitivity achieved by using AuNPs was verified by time-domain and frequency-domain measurements. The performance of the SH-SAW sensor was evaluated based on the values of $\Delta\alpha/k_0$ and $\Delta V/V$, and the performance of the LSPR sensor was evaluated based on the values of λ_P, $\Delta\lambda$, and S_r. Comprehensive experiments were performed using AFM, oscilloscope, VNA, and UV−vis spectrophotometry for surface imaging, time-domain evaluation, frequency-domain acousto-electric sensing characterization, and plasmonic sensing investigation, respectively. Thus, the SH-SAW sensor with AuNPs has a wide ε_r detection range (25−85), sensing capabilities for ultrasmall σ (0.00528−0.02504 S/m), and high sensitivity for n detection (45.5−201.9 nm/RIU). The cross-sectional effects were also evaluated. The effect of LSPR on the SH-SAW sensor was examined by turning the light OFF/ON. The impact of the SH-SAW sensor on LSPR was investigated

by turning the sine signal OFF/ON. We found that the SH-SAW sensor was not impacted by light. Interestingly, the presence of the SH-SAW sensor caused the AuNP position to vibrate and consistently generated a small blueshift in the LSPR effect. However, it did not significantly change the independent performance. In addition, for more general results, optimization to increase the velocity and enhance the sensitivity is needed. This could be achieved by varying the annealing temperature, quenching method, and size or structure of AuNPs and using different materials, such as silver (Ag). Then, its effect could be investigated by simulation or time-domain and frequency-domain measurements. Finally, the proposed hybrid multifunctional sensor was successfully developed by integrating two mature technologies and possessed several advantages, such as simultaneous detection with high sensitivity and independent characteristics, good stability in chemical environments, and the significant possibility of integration with a wireless network.

5. EXPERIMENTAL SECTION

5.1. SH-SAW Sensor. A 36XY-LiTaO$_3$ single crystal (Yamaju Ceramics Co. Ltd., Japan) was used as the piezoelectric substrate, as depicted in Figure S5(a). The preparation process was followed by cleaning the substrate using a paper wipe (Beamcot M-3II Asahi Kasei, Japan), 99.8 + % acetone liquid [(CH$_3$)$_2$CO] (Wako Pure Chemical Industries Ltd., Japan)], 99.9 + % 2-propanol (CH$_3$CHOHCH$_3$, Wako Pure Chemical Industries Ltd., Japan), and an ultrasonic cleaner (Branson Yamato 1200, Japan). Next, the substrate was dried using compressed air (Model CFD07B-8.5, Serial DM0428, Anest Iwata Co., Japan). This step was followed by the deposition of chromium and gold, as depicted in Figure S5(b,c), respectively. Chromium (99.99%, F-Company Japan) and gold metal materials (1.6 mm) with a diameter Ø of 1.0 mm (Tokuriki Honten Co. Ltd., Japan) were prepared and deposited using a vacuum thermal evaporator (VTE G-3, Chiyurikaki Kikai Seisakusho Co. Ltd., Japan).

To fabricate the IDTs, UV exposure and etching processes were utilized, as depicted in Figure S5(d,e), respectively. Before UV exposure, the device was cleaned using a N$_2$ gas blower (MD 920, Linicon, Japan). The process was followed by coating hexamethyldisilazane and a photoresist conductor (OFPR, Tokyo Ohka Kogyo Co. Ltd., Japan) using an active spin coater (ACT-220, Active Corp., Japan) and baking at a temperature of 115 °C using a hot plate (MH-180CS, As-one Ltd., Japan). The mask (Toyo PPM Corp., Japan) was covered with the device before UV exposure using an MJB UV-400 aligner (Suss Aligner 400). Subsequently, the device was baked again at a temperature of 115 °C. For the etching and development of the IDTs, an NMD-3 (Tokyo Ohka Kogyo Co. Ltd., Japan) liquid and a 99.8 + % [(CH$_3$)$_2$CO] acetone solution (Wako Pure Chemical Industries Ltd., Japan)] were utilized carefully and gently.

5.2. LSPR Sensor Based on the SH-SAW Sensor with AuNPs. To deposit AuNPs on the SH-SAW device, the IDTs should be masked, as illustrated in Figure S5(f). Gold (5.4 ± 0.1 mg, Ø = 0.5 mm) from Tokuriki Honten Co. Ltd., Japan, was deposited using VTE G-3 (Chiyurikaki Kikai Seisakusho Co. Ltd., Japan), as depicted in Figure S5(g). Thereafter, the mask was removed from the device, annealed at 500 °C for 5 min, and quenched to room temperature, as depicted in Figure S5(h). AuNPs were formed by a short annealing time and quenching[75] or annealing.[76] In addition, annealing and quenching can form a strong bond between the AuNPs and the substrate.[77−79] Therefore, repeatable measurements can be performed comfortably without worrying about the AuNPs being wiped away. The final proposed SH-SAW device with AuNPs is depicted in Figure S5(i).

5.3. Instrumentation Used for Measurement. As a liquid sample, 99.5 + % ethanol (C2H5OH) liquid (Wako Pure Chemical Industries Ltd., Japan) was used as a sample liquid at a concentration of 0−100 wt %. The conductivity was measured using a CM-40 S conductive system (CM Toa, Japan). For the physical and morphological investigation, an Eclipse E600 microscope (Nikon, Japan) was used to investigate the physical IDT structure. Morphology data were analyzed and visualized using AFM (SPA-400, Seiko Instrument Inc. (SII), Japan) and Gwyddion 2.55 software,[80] respectively. A vector network analyzer (43954A VNA HP Agilent, USA), WF1967 multifunction signal generator (NF Corporation, Japan), and InfiniVison MSKOX4033A high-precision oscilloscope (Keysight, USA) were utilized for SH-SAW sensor investigation and acoustoelectric evaluation. Finally, a light source (Model: 5−2300 unpolarized, Soma Optics, Ltd., Japan), USB4000 UV−vis spectrophotometer (Ocean Optics, Inc., USA), and OPwave + software were used for the LSPR sensor examination and characteristic measurements.

■ ASSOCIATED CONTENT

ⓢ Supporting Information

The Supporting Information is available free of charge at https://pubs.acs.org/doi/10.1021/acsami.1c00110.

Manufacturing process of the SH-SAW sensor without AuNPs and SH-SAW sensor with AuNPs and the peak reflection shifts at various voltages for various concentrations of EtOH (PDF)

■ AUTHOR INFORMATION

Corresponding Authors

Teguh Firmansyah − *Graduate School of Science and Technology, Shizuoka University, Hamamatsu-shi, Shizuoka 432-8561, Japan; Department of Electrical Engineering, Universitas Indonesia, Depok, West Java 16424, Indonesia;* orcid.org/0000-0002-9000-9337; Email: teguh.firmansyah81@ui.ac.id

Jun Kondoh − *Graduate School of Science and Technology and Graduate School of Integrated Science and Technology, Shizuoka University, Hamamatsu-shi, Shizuoka 432-8561, Japan;* Email: kondoh.jun@shizuoka.ac.jp

Authors

Gunawan Wibisono − *Department of Electrical Engineering, Universitas Indonesia, Depok, West Java 16424, Indonesia*

Eko Tjipto Rahardjo − *Department of Electrical Engineering, Universitas Indonesia, Depok, West Java 16424, Indonesia*

Complete contact information is available at:
https://pubs.acs.org/10.1021/acsami.1c00110

Author Contributions

The manuscript was written through contributions from all authors. All authors have approved the final version of the manuscript.

Notes

The authors declare no competing financial interest.

■ REFERENCES

(1) Petropoulou, A.; Kralj, S.; Karagiorgis, X.; Savva, I.; Loizides, E.; Panagi, M.; Krasia-Christoforou, T.; Riziotis, C. Multifunctional Gas and PH Fluorescent Sensors Based on Cellulose Acetate Electrospun Fibers Decorated with Rhodamine B-Functionalised Core-Shell Ferrous Nanoparticles. *Sci. Rep.* **2020**, *10*, 1−14.

(2) Kulkarni, M. R.; John, R. A.; Rajput, M.; Tiwari, N.; Yantara, N.; Nguyen, A. C.; Mathews, N. Transparent Flexible Multifunctional Nanostructured Architectures for Non-Optical Readout, Proximity, and Pressure Sensing. *ACS Appl. Mater. Interfaces* **2017**, *9*, 15015−15021.

(3) Gu, J.; Huang, J.; Chen, G.; Hou, L.; Zhang, J.; Zhang, X.; Yang, X.; Guan, L.; Jiang, X.; Liu, H. Multifunctional Poly(Vinyl Alcohol) Nanocomposite Organohydrogel for Flexible Strain and Temperature Sensor. *ACS Appl. Mater. Interfaces* **2020**, *12*, 40815−40827.

(4) Ershad, F.; Thukral, A.; Yue, J.; Comeaux, P.; Lu, Y.; Shim, H.; Sim, K.; Kim, N. I.; Rao, Z.; Guevara, R.; Contreras, L.; Pan, F.; Zhang, Y.; Guan, Y. S.; Yang, P.; Wang, X.; Wang, P.; Wu, X.; Yu, C. Ultra-Conformal Drawn-on-Skin Electronics for Multifunctional Motion Artifact-Free Sensing and Point-of-Care Treatment. *Nat. Commun.* **2020**, *11*, 1−13.

(5) Majumder, B. D.; Roy, J. K.; Padhee, S. Recent Advances in Multifunctional Sensing Technology on a Perspective of Multi-Sensor System: A Review. *IEEE Sens. J.* **2019**, *19*, 1204−1214.

(6) Lendlein, A.; Trask, R. S. Multifunctional Materials: Concepts, Function-Structure Relationships, Knowledge-Based Design, Translational Materials Research. *Multifunct. Mater.* **2018**, *1*, No. 010201.

(7) Nakata, S.; Arie, T.; Akita, S.; Takei, K. Wearable, Flexible, and Multifunctional Healthcare Device with an ISFET Chemical Sensor for Simultaneous Sweat PH and Skin Temperature Monitoring. *ACS Sensors* **2017**, *2*, 443−448.

(8) Liu, H.; Wang, X.; Cao, Y.; Yang, Y.; Yang, Y.; Gao, Y.; Ma, Z.; Wang, J.; Wang, W.; Wu, D. Freezing-Tolerant, Highly Sensitive Strain and Pressure Sensors Assembled from Ionic Conductive Hydrogels with Dynamic Cross-Links. *ACS Appl. Mater. Interfaces* **2020**, *12*, 25334−25344.

(9) Wang, R.; Wang, X.; Sun, Y. One-Step Synthesis of Self-Doped Carbon Dots with Highly Photoluminescence as Multifunctional Biosensors for Detection of Iron Ions and PH. *Sens. Actuators, B* **2017**, *241*, 73−79.

(10) Wu, J.; Wu, Z.; Ding, H.; Wei, Y.; Yang, X.; Li, Z.; Yang, B. R.; Liu, C.; Qiu, L.; Wang, X. Multifunctional and High-Sensitive Sensor Capable of Detecting Humidity, Temperature, and Flow Stimuli Using an Integrated Microheater. *ACS Appl. Mater. Interfaces* **2019**, *11*, 43383−43392.

(11) Huang, L.; Zhang, Z.; Li, Z.; Chen, B.; Ma, X.; Dong, L.; Peng, L. M. Multifunctional Graphene Sensors for Magnetic and Hydrogen Detection. *ACS Appl. Mater. Interfaces* **2015**, *7*, 9581−9588.

(12) Liu, Y.; Zhang, D. Synergetic Effect in the Multifunctional Composite Film of Graphene-TiO2with Transparent Conductive, Photocatalytic and Strain Sensing Properties. *J. Alloys Compd.* **2017**, *698*, 60−67.

(13) Park, C. H.; Yang, H.; Lee, J.; Cho, H. H.; Kim, D.; Lee, D. C.; Kim, B. J. Multicolor Emitting Block Copolymer-Integrated Graphene Quantum Dots for Colorimetric, Simultaneous Sensing of Temperature, PH, and Metal Ions. *Chem. Mater.* **2015**, *27*, 5288−5294.

(14) Shin, S. H.; Park, D. H.; Jung, J. Y.; Lee, M. H.; Nah, J. Ferroelectric Zinc Oxide Nanowire Embedded Flexible Sensor for Motion and Temperature Sensing. *ACS Appl. Mater. Interfaces* **2017**, *9*, 9233−9238.

(15) Rabus, D.; Friedt, J. M.; Arapan, L.; Lamare, S.; Baqué, M.; Audouin, G.; Chérioux, F. Subsurface H2S Detection by a Surface Acoustic Wave Passive Wireless Sensor Interrogated with a Ground Penetrating Radar. *ACS Sensors* **2020**, *5*, 1075−1081.

(16) Hunge, Y. M.; Yadav, A. A.; Kulkarni, S. B.; Mathe, V. L. A Multifunctional ZnO Thin Film Based Devises for Photoelectrocatalytic Degradation of Terephthalic Acid and CO2 Gas Sensing Applications. *Sens. Actuators, B* **2018**, *274*, 1−9.

(17) Tao, R.; Zahertar, S.; Torun, H.; Liu, Y. R.; Wang, M.; Lu, Y.; Luo, J. T.; Vernon, J.; Binns, R.; He, Y.; Tao, K.; Wu, Q.; Chang, H. L.; Fu, Y. Q. Flexible and Integrated Sensing Platform of Acoustic Waves and Metamaterials Based on Polyimide-Coated Woven Carbon Fibers. *ACS sensors* **2020**, *5*, 2563−2569.

(18) Pedro, J.; Zhao, X. B.; Ashley, G. M.; Flewitt, A. J.; Garcıı, L.; Milne, W. I.; Ford, C. J. B.; Lu, J. R.; Luo, J. K. Dual-Mode Thin Film Bulk Acoustic Wave Resonators for Parallel Sensing of Temperature and Mass Loading. *Biosens. Bioelectron.* **2012**, *38*, 369−374.

(19) Sternhagen, J. D.; Wold, C. E.; Kempf, W. A.; Karlgaard, M.; Mitzner, K. D.; Mileham, R. D.; Galipeau, D. W. A Novel Integrated Acoustic Gas and Temperature Sensor. *IEEE Sens. J.* **2002**, *2*, 301−306.

(20) Hao, D.; Hu, C.; Grant, J.; Glidle, A.; Cumming, D. R. S. Hybrid Localized Surface Plasmon Resonance and Quartz Crystal Microbalance Sensor for Label Free Biosensing. *Biosens. Bioelectron.* **2018**, *100*, 23−27.

(21) Friedt, J. M.; Francis, L. A. Combined Surface Acoustic Wave and Surface Plasmon Resonance Measurement of Collagen and Fibrinogen Layer Physical Properties. *Sens. Bio-Sensing Res.* **2016**, *11*, 60−70.

(22) Binder, A.; Bruckner, G.; Schobernig, N.; Schmitt, D. Wireless Surface Acoustic Wave Pressure and Temperature Sensor with Unique Identification Based on LiNbO3. *IEEE Sens. J.* **2013**, *13*, 1801−1805.

(23) Li, B.; Member, S.; Yassine, O.; Kosel, J.; Member, S. A. Surface Acoustic Wave Passive and Wireless Sensor for Magnetic Fields, Temperature, and Humidity. *IEEE Sens. J.* **2015**, *15*, 453−462.

(24) Renaudin, A.; Chabot, V.; Grondin, E.; Aimez, V.; Charette, P. G. Integrated Active Mixing and Biosensing Using Surface Acoustic Waves (SAW) and Surface Plasmon Resonance (SPR) on a Common Substrate. *Lab Chip* **2010**, *10*, 111−115.

(25) Müller, A.; Konstantinidis, G.; Giangu, I.; Adam, G. C.; Stefanescu, A.; Stavrinidis, A.; Stavrinidis, G.; Kostopoulos, A.; Boldeiu, G.; Dinescu, A. GaN Membrane Supported SAW Pressure Sensors With Embedded Temperature Sensing Capability. *IEEE Sens. J.* **2017**, *17*, 7383−7393.

(26) Narushima, A.; Genji, T.; Kondoh, J. Combination of a Surface Acoustic Wave Device and Classical Sensor for Detecting Physical Quantity 1- Simultaneous Detection Method of Physical Quantity and Temperature. *In Proceedings of Symposium on Ultrasonic Electronics*; 2012, *33*, 67−68.

(27) Kobayashi, S.; Kondoh, J. Feasibility Study on Shear Horizontal Surface Acoustic Wave Sensors for Engine Oil Evaluation. *Sensors (Switzerland)* **2020**, *20*, No. 21840.

(28) Okuda, S.; Ono, T.; Kanai, Y.; Ikuta, T.; Shimatani, M.; Ogawa, S.; Maehashi, K.; Inoue, K.; Matsumoto, K. Graphene Surface Acoustic Wave Sensor for Simultaneous Detection of Charge and Mass. *ACS Sensors* **2017**, *3*, 200−204.

(29) Kondoh, J.; Shiokawa, S. Measurements of Conductivity and Ph of Liquid Using Surface Acoustic Wave Devices. *In Proceedings of 12th Symposium on Ultrasonic Electronics*; Tokyo, 1991; 82−84.

(30) Kondoh, J.; Hayashi, S.; Shiokawa, S. Simultaneous Detection of Density and Viscosity Using Surface Acoustic Wave Liquid-Phase Sensors. *Jpn J. Appl. Phys* **2001**, *40*, 3713−3717.

(31) Chen, Z.; Zhou, J.; Tang, H.; Liu, Y.; Shen, Y.; Yin, X.; Zheng, J.; Zhang, H.; Wu, J.; Shi, X.; Chen, Y.; Fu, Y.; Duan, H. Ultrahigh-Frequency Surface Acoustic Wave Sensors with Giant Mass-Loading Effects on Electrodes. *ACS Sensors* **2020**, *5*, 1657−1664.

(32) Shiokawa, S.; Kondoh, J. Surface Acoustic Wave Sensor for Liquid-Phase Application. *IEEE Ultrason. Symp.* **1999**, 445−452.

(33) Shiokawa, S.; Kondoh, J. Surface Acoustic Wave Microsensors. *Electron. Commun. Japan, Pt II* **1996**, *79*, 42−50.

(34) Kondoh, J.; Shiokawa, S. SH-SAW Taste Sensor Based Acoustoelectric Interaction. *Proc. IEEE Ultrason. Symp.* **1993**, *1*, 421−424.

(35) Kondoh, J.; Shiokawa, S. Identification of Liquid Samples Using Shear-horizontal Surface Acoustic Wave Sensors. *Electron. Commun. Jpn Pt II* **1995**, *78*, 50−59.

(36) Fu, Y. Q.; Luo, J. K.; Nguyen, N. T.; Walton, A. J.; Flewitt, A. J.; Zu, X. T.; Li, Y.; McHale, G.; Matthews, A.; Iborra, E.; Du, H.; Milne, W. I. Advances in Piezoelectric Thin Films for Acoustic Biosensors, Acoustofluidics and Lab-on-Chip Applications. *Prog. Mater. Sci.* **2017**, *89*, 31−91.

(37) Newman, T.; Josse, F.; Mensah-Brown, A.; Bender, F. Analysis of the Detection of Organophosphate Pesticides in Aqueous Solutions Using Polymer-Coated SH-SAW Sensor Arrays. *IEEE Sens. J.* **2013**, *12*, 893−902.

(38) Mensah-Brown, A. K.; Mlambo, D.; Josse, F.; Schneider, S. C. Analysis of the Detection of Organophosphate Pesticides in Aqueous Solutions Using Hydrogen-Bond Acidic Coating on SH-SAW Devices. *IEEE Sens. J.* **2012**, *12*, 893−903.

(39) Kondoh, J.; Shiokawa, S. A. Liquid Sensor Based on a Shear Horizontal Saw Device. *Electron. Commun. Jpn Pt II* **1993**, *76*, 69−82.

(40) Kondoh, J.; Shiokawa, S. Shear Surface Acoustic Wave Liquid Sensor Based on Acoustoelectric Interaction. *Electron Commun. Jpn Pt II.* **1995**, *78*, 101−112.

(41) Bohren, C. F.; Huffman, D. R. *Absorption and Scattering of Light by Small Particles*; Wiley-Interscience: New York, 1998.

(42) Mayer, K. M.; Hafner, J. H. Localized Surface Plasmon Resonance Sensors. *Chem. Rev.* **2011**, *111*, 3828−3857.

(43) Geng, Z.; Kan, Q.; Yuan, J.; Chen, H. A Route to Low-Cost Nanoplasmonic Biosensor Integrated with Optofluidic-Portable Platform. *Sens. Actuators, B* **2014**, *195*, 682−691.

(44) Bonyar, A.; Wimmer, B.; Csarnovics, I. Development of a Localised Surface Plasmon Resonance Sensor Based on Gold Nanoparticles. *Proc. 2014 37th Int. Spring Semin. Electron. Technol. ISSE 2014* **2014**, 369−374.

(45) Karakouz, T.; Maoz, B. M.; Lando, G.; Vaskevich, A.; Rubinstein, I. Stabilization of Gold Nanoparticle Films on Glass by Thermal Embedding. *ACS Appl. Mater. Interfaces* **2011**, *3*, 978−987.

(46) Kedem, O.; Vaskevich, A.; Rubinstein, I. Improved Sensitivity of Localized Surface Plasmon Resonance Transducers Using Reflection Measurements. *J. Phys. Chem. Lett.* **2011**, *2*, 1223−1226.

(47) Szunerits, S.; Boukherroub, R. Sensing Using Localised Surface Plasmon Resonance Sensors. *Chem. Commun.* **2012**, *48*, 8999−9010.

(48) Willets, K. A.; Van Duyne, R. P. Localized Surface Plasmon Resonance Spectroscopy and Sensing. *Annu. Rev. Phys. Chem.* **2007**, *58*, 267−297.

(49) Anker, J. N.; Hall, W. P.; Lyandres, O.; Shah, N. C.; Zhao, J.; Van Duyne, R. P. Biosensing with Plasmonic Nanosensors. *Nat. Mater.* **2009**, *7*, 308−319.

(50) Chen, J.; Xu, R.; Yan, Z.; Tang, C.; Chen, Z.; Wang, Z. Preparation of Metallic Triangular Nanoparticle Array with Control-lable Interparticle Distance and Its Application in Surface-Enhanced Raman Spectroscopy. *Opt. Commun.* **2013**, *307*, 73−75.

(51) Mokkath, J. H. Nanoparticle Heterodimers: The Role of Size and Interparticle Gap Distance on the Optical Response. *Chem. Phys. Lett.* **2018**, *699*, 28−31.

(52) Cortijo-Campos, S.; Ramírez-Jiménez, R.; Climent-Pascual, E.; Aguilar-Pujol, M.; Jiménez-Villacorta, F.; Martínez, L.; Jiménez-Riobóo, R.; Prieto, C.; de Andrés, A. Raman Amplification in the Ultra-Small Limit of Ag Nanoparticles on SiO2 and Graphene: Size and Inter-Particle Distance Effects. *Mater. Des.* **2020**, *192*, No. 108702.

(53) Mizuno, A.; Ono, A. Static and Dynamic Tuning of Surface Plasmon Resonance by Controlling Interparticle Distance in Arrays of Au Nanoparticles. *Appl. Surf. Sci.* **2019**, *480*, 846−850.

(54) Song, Y.; Tran, V. T.; Lee, J. Tuning Plasmon Resonance in Magnetoplasmonic Nanochains by Controlling Polarization and Interparticle Distance for Simple Preparation of Optical Filters. *ACS Appl. Mater. Interfaces* **2017**, *9*, 24433−24439.

(55) Mansoor, R.; AL-Khursan, A. H. Numerical Modelling of Surface Plasmonic Polaritons. *Results Phys.* **2018**, *9*, 1297−1300.

(56) Proietti Zaccaria, R.; Bisio, F.; Das, G.; Maidecchi, G.; Caminale, M.; Vu, C. D.; De Angelis, F.; Di Fabrizio, E.; Toma, A.; Canepa, M. Plasmonic Color-Graded Nanosystems with Achromatic

(57) Subwavelength Architectures for Light Filtering and Advanced SERS Detection. *ACS Appl. Mater. Interfaces* **2016**, *8*, 8024−8031.

(57) Refractive index database https://refractiveindex.info (accessed Jul 10, 2020).

(58) Firmansyah, T.; Praptodinoyo, S.; Wiryadinata, R.; Suhendar, S.; Wardoyo, S.; Alimuddin, A.; Chairunissa, C.; Alaydrus, M.; Wibisono, G. Dual-Wideband Band Pass Filter Using Folded Cross-Stub Stepped Impedance Resonator. *Microw. Opt. Technol. Lett.* **2017**, *59*, 2929.

(59) Firmansyah, T.; Alaydrus, M.; Wahyu, Y.; Rahardjo, E. T.; Wibisono, G. A Highly Independent Multiband Bandpass Filter Using a Multi-Coupled Line Stub-Sir with Folding Structure. *IEEE Access* **2020**, *8*, 83009−83026.

(60) Kogai, T.; Yatsuda, H.; Kondoh, J. Rayleigh SAW-Assisted SH-SAW Immunosensor on X-Cut 148-Y LiTaO3. *IEEE Trans. Ultrason. Ferroelectr. Freq. Control* **2017**, *64*, 1375−1381.

(61) Firmansyah, T.; Praptodiyono, S.; Pramudyo, A. S.; Chairunissa, C.; Alaydrus, M. Hepta-Band Bandpass Filter Based on Folded Cross-Loaded Stepped Impedance Resonator. *Electron. Lett.* **2017**, *53*, 1119.

(62) Haynes, W. M. *Handbook of Chemistry and Physics*, 2016th ed.; CRC Press, 2016; *4*.

(63) Lee, M. H.; Kim, D. J.; Choi, H. I.; Kim, M.-H.; Song, T. K.; Kim, W.-J.; Do, D. Thermal Quenching Effects on the Ferroelectric and Piezoelectric Properties of BiFeO 3 −BaTiO 3 Ceramics. *ACS Appl. Electron. Mater.* **2019**, *1*, 1772−1780.

(64) Phan, D. T.; Chung, G. S. Effects of Rapid Thermal Annealing on Surface Acoustic Wave Ultraviolet Sensors Using ZnO Nanorods Grown on AlN/Si Structures. *J. Electroceram.* **2013**, *30*, 185−190.

(65) Rimeika, R.; Ciplys, D. Influence of Annealing on Electro-mechanical Coupling Coefficient in Proton Exchanged 128° Rotated Y-X LiNbO3. *Phys. Status Solidi Appl. Res.* **1998**, *168*, 65−66.

(66) Yamashita, K.; Nakajima, S.; Shiomi, J.; Noda, M. Sensitivity of Piezoelectric Ultrasonic Microsensors with Sol-Gel Derived PZT Films Prepared through Various Pyrolysis Temperatures. *Proceedings* **2017**, *1*, 394.

(67) Zhukov, R. N.; Kushnerev, K. S.; Kiselev, D. A.; Ilina, T. S.; Kubasov, I. V.; Kislyuk, A. M.; Malinkovich, M. D.; Parkhomenko, Y. N. Enhancement of Piezoelectric Properties of Lithium Niobate Thin Films by Different Annealing Parameters. *Mod. Electron. Mater.* **2020**, *6*, 47−52.

(68) Richardson, M.; Sankaranarayanan, S. K. R. S.; Bhethanabotla, V. R. Low Insertion Loss and Highly Sensitive SH-SAW Sensors Based on 36° YX LiTaO3 through the Incorporation of Filled Microcavities. *IEEE Sens. J.* **2015**, *15*, 787−796.

(69) Irani, F. S.; Tunaboylu, B. SAW Humidity Sensor Sensitivity Enhancement via Electrospraying of Silver Nanowires. *Sensors (Switzerland)* **2016**, *16*, 1−8.

(70) Cular, S.; Sankaranarayanan, S. K. R. S.; Bhethanabotla, V. R. Enhancing Effects of Microcavities on Shear-Horizontal Surface Acoustic Wave Sensors: A Finite Element Simulation Study. *Appl. Phys. Lett.* **2008**, *92*, 244104.

(71) Mohanan, A. A.; Ramakrishnan, N. Investigation into Effect of Coupled Resonance Phenomenon towards Sensitivity Enhancement of SAW Conductivity Sensors Integrated with ZnO Nanorods. *Microsyst. Technol.* **2020**, *26*, 2075−2086.

(72) Guo, L.; Jackman, J. A.; Yang, H. H.; Chen, P.; Cho, N. J.; Kim, D. H. Strategies for Enhancing the Sensitivity of Plasmonic Nanosensors. *Nano Today* **2015**, *10*, 213−239.

(73) Chen, H.; Kou, X.; Yang, Z.; Ni, W.; Wang, J. Shape- and Size-Dependent Refractive Index Sensitivity of Gold Nanoparticles. *Langmuir* **2008**, *24*, 5233−5237.

(74) Jeon, H. B.; Tsalu, P. V.; Ha, J. W. Shape Effect on the Refractive Index Sensitivity at Localized Surface Plasmon Resonance Inflection Points of Single Gold Nanocubes with Vertices. *Sci. Rep.* **2019**, *9*, 1−8.

(75) Handoyo, T.; Kondoh, J. Enhancement of Ultrathin Localized Surface Plasmon Resonance Sensitivity Using Sequential Temperature

Treatment for Liquids Sensing. *Sensors Actuators, A Phys.* **2020**, *307*, No. 112006.

(76) Karakouz, T.; Holder, D.; Goomanovsky, M.; Vaskevich, A.; Rubinstein, I. Morphology and Refractive Index Sensitivity of Gold Island Films. *Chem. Mater.* **2009**, *21*, 5875−5885.

(77) Kobayashi, Y.; Maeda, T.; Yasuda, Y.; Morita, T. Metal−Metal Bonding Using Silver/Copper Nanoparticles. *Appl. Nanosci.* **2016**, *6*, 883−893.

(78) Fu, X.; Wang, R.; Zhu, Q.; Wang, P.; Zuo, Y. Effect of Annealing on the Interface and Mechanical Properties of Cu-Al-Cu Laminated Composite Prepared with Cold Rolling. *Materials* **2020**, *13*, 369.

(79) Tseng, Y. W.; Hung, F. Y.; Lui, T. S.; Chen, M. Y.; Hsueh, H. W. Effect of Annealing on the Microstructure and Bonding Interface Properties of Ag-2Pd Alloy Wire. *Microelectron. Reliab.* **2015**, *55*, 1256−1261.

(80) http://gwyddion.net/ (accessed Apr 17, 2020).

Multifunctional and Sensitivity Enhancement of Hybrid Acoustoplasmonic Sensors Fabricated on 36XY-LiTaO

1 "Handbook of Nanocelluloses", Springer Science and Business Media LLC, 2022
Publication
1%

2 Teguh Handoyo, Jun Kondoh. "Enhancement of ultrathin localized surface plasmon resonance sensitivity using sequential temperature treatment for liquids sensing", Sensors and Actuators A: Physical, 2020
Publication
1%

3 epublications.marquette.edu
Internet Source
1%

4 irep.ntu.ac.uk
Internet Source
1%

5 www.osti.gov
Internet Source
1%

6 shizuoka.repo.nii.ac.jp
Internet Source
1%

7 Andrew P Campitelli, Wojciech Wlodarski, Moussa Hoummady. "Identification of natural
1%

spring water using shear horizontal SAW based sensors", Sensors and Actuators B: Chemical, 1998
Publication

8   www.mdpi.com   1%
     Internet Source

9   Kyosuke Tada, Takuya Nozawa, Jun Kondoh.   <1%
     "Real-time monitoring of methanol
     concentration using a shear horizontal
     surface acoustic wave sensor for direct
     methanol fuel cell without reference liquid
     measurement", Japanese Journal of Applied
     Physics, 2017
     Publication

10   Kento Ueda, Jun Kondoh. "Estimation of liquid   <1%
     properties by inverse problem analysis based
     on shear horizontal surface acoustic wave
     sensor responses", Japanese Journal of
     Applied Physics, 2017
     Publication

11   aip.scitation.org   <1%
     Internet Source

12   www.bph.rub.de   <1%
     Internet Source

13   wrap.warwick.ac.uk   <1%
     Internet Source

14 Sergio Alejandro Poveda Cuevas. "Structural Bioinformatics studies of the Zika virus non-structural protein 1 and its molecular interactions", Universidade de Sao Paulo, Agencia USP de Gestao da Informacao Academica (AGUIA), 2022
Publication

<1%

15 www.binn.cas.cn
Internet Source

<1%

16 iopscience.iop.org
Internet Source

<1%

17 research-repository.griffith.edu.au
Internet Source

<1%

18 Thomas Lee, S.. "Long period gratings in multimode optical fibers: application in chemical sensing", Optics Communications, 20030901
Publication

<1%

19 xvilaysouk.github.io
Internet Source

<1%

20 Jun Kondoh, Takuya Nozawa. "Online real-time monitoring method of methanol concentration for direct methanol fuel cell using shear horizontal surface acoustic wave", 2014 IEEE International Ultrasonics Symposium, 2014
Publication

<1%

21 Jun Kondoh, Tomohiko Fukaya. "Experimental considerations of droplet manipulation mechanism using surface acoustic wave devices", Acoustical Society of America (ASA), 2018
Publication
<1%

22 repositorio.uchile.cl
Internet Source
<1%

23 www.diva-portal.se
Internet Source
<1%

24 Campitelli, A.P.. "Identification of natural spring water using shear horizontal SAW based sensors", Sensors & Actuators: B. Chemical, 19980701
Publication
<1%

25 Jun Kondoh, Kazuki Nakayama, Iren Kuznetsova. "Study of frequency dependence of shear horizontal surface acoustic wave sensor for engine oil measurements", Sensors and Actuators A: Physical, 2021
Publication
<1%

26 Jun Kondoh. "A liquid-phase sensor using shear horizontal surface acoustic wave devices", Electronics and Communications in Japan, 2013
Publication
<1%

27   Kondoh, J.. "Development of practical surface acoustic wave liquid sensing system and its application for measurement of Japanese tea", Sensors & Actuators: B. Chemical, 20030701
Publication   <1 %

28   Mitsakakis, K.. "Parametric study of SH-SAW device response to various types of surface perturbations", Sensors & Actuators: B. Chemical, 20090506
Publication   <1 %

29   S. Shiokawa. "Interaction of surface acoustic waves and particles", IEEE Ultrasonics Symposium 2005, 2005
Publication   <1 %

30   Jun Kondoh. "Shear surface acoustic wave liquid sensor based on acoustoelectric interaction", Electronics and Communications in Japan (Part II Electronics), 01/1995
Publication   <1 %

31   Paromita Bhattacharjee, Himakshi Mishra, Parameswar Krishnan Iyer, Harshal Bhalchandra Nemade. "Acoustically Assisted Charge Transport in Poly(3-hexylthiophene)", ACS Applied Electronic Materials, 2022
Publication   <1 %

32 Andreas Steinegger, Otto S. Wolfbeis, Sergey M. Borisov. "Optical Sensing and Imaging of pH Values: Spectroscopies, Materials, and Applications", Chemical Reviews, 2020
Publication

<1 %

33 Joshi, Gayatri K., Phillip J. McClory, Barry B. Muhoberac, Amar Kumbhar, Kimberly A. Smith, and Rajesh Sardar. "Designing Efficient Localized Surface Plasmon Resonance-Based Sensing Platforms: Optimization of Sensor Response by Controlling the Edge Length of Gold Nanoprisms", The Journal of Physical Chemistry C, 2012.
Publication

<1 %

34 Matthew E. Stewart, Christopher R. Anderton, Lucas B. Thompson, Joana Maria, Stephen K. Gray, John A. Rogers, Ralph G. Nuzzo. "Nanostructured Plasmonic Sensors", Chemical Reviews, 2008
Publication

<1 %

35 Saya Kobayashi, Jun Kondoh. "Feasibility Study on Shear Horizontal Surface Acoustic Wave Sensors for Engine Oil Evaluation", Sensors, 2020
Publication

<1 %

36 Muhammad Syahmi Abd Rahman, Mohd Zainal Abidin Ab Kadir, Muhamad Safwan Ab-Rahman, Miszaina Osman et al. "Effects of a

<1 %

Crossarm Brace Application on a 275 kV Fiberglass-Reinforced Polymer Crossarm Subjected to a Lightning Impulse", Energies, 2020
Publication

37 kipdf.com
Internet Source
<1 %

38 Guo-Yang Li, Guoqiang Xu, Yang Zheng, Yanping Cao. "Non-leaky modes and bandgaps of surface acoustic waves in wrinkled stiff-film/compliant-substrate bilayers", Journal of the Mechanics and Physics of Solids, 2018
Publication
<1 %

39 Henny Suzana Mediani, Risnawaty Risnawaty, Ai Mardhiyah. "Effect of Psychoeducation Intervention on Self-efficacy and Coping of Adolescent Thalassemic Survivors in Indonesia", Global Journal of Health Science, 2021
Publication
<1 %

40 bmjopen.bmj.com
Internet Source
<1 %

41 Fabien Josse, Florian Bender, Richard W. Cernosek. "Guided Shear Horizontal Surface Acoustic Wave Sensors for Chemical and Biochemical Detection in Liquids", Analytical Chemistry, 2001
<1 %

42   Xuan Dai, Lili Fang, Chuanfang Zhang, Houjun Sun. "An Impedance-Loaded Orthogonal Frequency-Coded SAW Sensor for Passive Wireless Sensor Networks", Sensors, 2020
Publication

<1 %

43   Yuanyuan Li, Jian Yang, Bei Jiang, Le Cao, Xiangyi Shen, Meng Shao. "Finite element simulation for sensitivity measurement of a shear horizontal surface acoustic wave micro pressure sensor with a groove structure", Measurement Science and Technology, 2021
Publication

<1 %

44   www.nature.com
Internet Source

<1 %

45   Hongyuan Zhao, Shuangqing Fan, Yan Chen, Zhihong Feng, Hao Zhang, Wei Pang, Daihua Zhang, Menglun Zhang. "Oxygen Plasma-Treated Graphene Oxide Surface Functionalization for Sensitivity Enhancement of Thin-Film Piezoelectric Acoustic Gas Sensors", ACS Applied Materials & Interfaces, 2017
Publication

<1 %

46   S. Shiokawa. "Measurements of particles in liquid using surface acoustic wave sensors", Proceedings of the 2004 IEEE International

<1 %

Frequency Control Symposium and Exposition 2004, 2004
Publication

47 Yue Yang, Xuechun Xiao, Xinxin Xing, Zhezhe Wang, Tong Zou, Zidong Wang, Rongjun Zhao, Yude Wang. "Rhodamine B assisted graphene quantum dots flourescent sensor system for sensitive recognition of mercury ions", Journal of Luminescence, 2019
Publication
<1 %

48 archiv.ub.uni-heidelberg.de
Internet Source
<1 %

49 gyan.iitg.ernet.in
Internet Source
<1 %

50 innovareacademics.in
Internet Source
<1 %

51 pld.nju.edu.cn
Internet Source
<1 %

52 www.science.gov
Internet Source
<1 %

53 Bing Wang, Yizhe Li, David A. Hall. "Surface structure and quenching effects in BiFeO3 - BaTiO3 ceramics", Journal of the American Ceramic Society, 2021
Publication
<1 %

54 Davide Santoro, Lukas Winter, Alexander Müller, Julia Vogt et al. "Detailing Radio Frequency Heating Induced by Coronary Stents: A 7.0 Tesla Magnetic Resonance Study", PLoS ONE, 2012
Publication

<1 %

55 E. Berkenpas, S. Bitla, P. Millard, M. Pereira da Cunha. "Pure shear horizontal SAW biosensor on langasite", IEEE Transactions on Ultrasonics, Ferroelectrics and Frequency Control, 2004
Publication

<1 %

56 Hemant Jatav, Masoud Shabaninezhad, Maja Mičetić, Anusmita Chakravorty et al. "A Combinatorial Study Investigating the Growth of Ultrasmall Embedded Silver Nanoparticles upon Thermal Annealing", Langmuir, 2022
Publication

<1 %

57 Mohanan, Ajay Achath, R Parthiban, and N Ramakrishnan. "Shadow mask assisted direct growth of ZnO nanowires as a sensing medium for surface acoustic wave devices using a thermal evaporation method", Journal of Micromechanics and Microengineering, 2016.
Publication

<1 %

58 Pang, Hua Feng, Kai Min Fan, Yong Qing Fu, Frank Placido, Jin Yi Ma, and Xiao Tao Zu.

<1 %

"Droplet Streaming and Nebulization Induced by the Shear Horizontal Surface Acoustic Wave", Advanced Materials Research, 2013.
Publication

59   Qinglin Li, Jiawen Chen, Yuxia Zhang, Chongyi Chi, Guofa Dong, Jianrong Lin, Qinhui Chen. "Superelastic, Antifreezing, Antidrying, and Conductive Organohydrogels for Wearable Strain Sensors", ACS Applied Materials & Interfaces, 2021   <1 %
Publication

60   Stefany Jacesko. "Investigations on an electronic tongue with polymer microfluidic cell for liquid sensing and identification", Smart Materials and Structures, 10/01/2005   <1 %
Publication

61   Teguh Handoyo, Jun Kondoh. "Characterization of self-assembled AuNPs film for optofluidic applications", 2018 4th International Conference on Nano Electronics Research and Education (ICNERE), 2018   <1 %
Publication

62   Xiang Tao, Hao Jin, Mona Mintken, Niklas Wolff et al. "Three-Dimensional Tetrapodal ZnO Microstructured Network Based Flexible Surface Acoustic Wave Device for Ultraviolet and Respiration Monitoring Applications", ACS Applied Nano Materials, 2020   <1 %
Publication

63 jianhui wu, Changshuai Yin, Jian Zhou, Honglang Li, Yi Liu, Yiping Shen, Sean Garner, Yongqing Fu, Huigao Duan. "Ultra-thin Glass Based Flexible, Transparent and Ultra-sensitive Surface Acoustic Wave Humidity Sensor with ZnO Nanowires and Graphene Quantum Dots", ACS Applied Materials & Interfaces, 2020
Publication

<1 %

64 osuva.uwasa.fi
Internet Source

<1 %

65 scholar.uwindsor.ca
Internet Source

<1 %

66 thinkmind.org
Internet Source

<1 %

67 www.forestbioproducts.umaine.edu
Internet Source

<1 %

68 www.te.chiba-u.jp
Internet Source

<1 %

69 Jun Kondoh, Yoshikazu Matsui, Showko Shiokawa. "Identification of electrolyte solutions using a shear horizontal surface acoustic wave sensor with a liquid-flow system", Sensors and Actuators B: Chemical, 2003
Publication

<1 %

70	"Nanoplasmonic Sensors", Springer Nature, 2012 Publication	<1 %
71	doaj.org Internet Source	<1 %

Exclude quotes   Off   Exclude matches   Off
Exclude bibliography On